LA-9262-PR

Progress Report

Los Alamos National Laboratory is operated by the University of California for the United States Department of Energy under contract W-7405-ENG-36.

Applied Nuclear Data Research and Development

July 1—September 30, 1981

Los Alamos National Laboratory
Los Alamos, New Mexico 87545

The four most recent reports in this series, unclassified, are LA-8630-PR, LA-8757-PR, LA-8874-PR, and LA-9060-PR.

This work was performed under the auspices of the US Department of Energy's Division of Reactor Research and Technology, Office of Basic Energy Sciences, Office of Fusion Energy; the Spent Fuel Project Office under the technical direction of the Savannah River Laboratory; the Electric Power Research Institute; and the Nuclear Regulatory Commission.

LA-9262-PR
Progress Report

UC-34c
Issued: March 1982

Applied Nuclear Data Research and Development

July 1—September 30, 1981

Compiled by
P. G. Young

Los Alamos National Laboratory
Los Alamos, New Mexico 87545

CONTENTS

APPLIED NUCLEAR DATA RESEARCH AND DEVELOPMENT
QUARTERLY PROGRESS REPORT
July 1 - September 30, 1981

Compiled by

P. G. Young

ABSTRACT

This progress report describes the activities of the Los Alamos Nuclear Data Group for July 1 through September 30, 1981. The topical content is summarized in the Table of Contents.

I. THEORY AND EVALUATION OF NUCLEAR CROSS SECTIONS

A. Calculations of Neutron Spectra from the n+d Reaction* (G. M. Hale)

Spectra for light-particle reactions leading to three-body final states are important in many applications because such reactions can occur at relatively low energies. Typically, these spectra consist of relatively narrow peaks on top of broad, underlying structures commonly attributed to "three-body-phase space" contributions. However, such structure can also come from kinematically broadened resonance effects, as, for instance, the contribution from the n-α resonance in the ^{6}Li(n,n')dα spectra calculations described in a previous report.[1]

We have calculated neutron spectra from the n+d reaction using a resonance model similar to that described in Ref. 1, except that interference between the direct and exchange amplitudes has been taken into account, and an approximate integral of the exchange contribution over the angles of the undetected particle has been replaced by the exact expression. The calculations for 14.1-MeV incident neutrons are compared in Fig. 1 with spectra measured at two laboratory

---

*Much of this work was done while at Centre d'Études de Bruyères-le-Châtel, France.

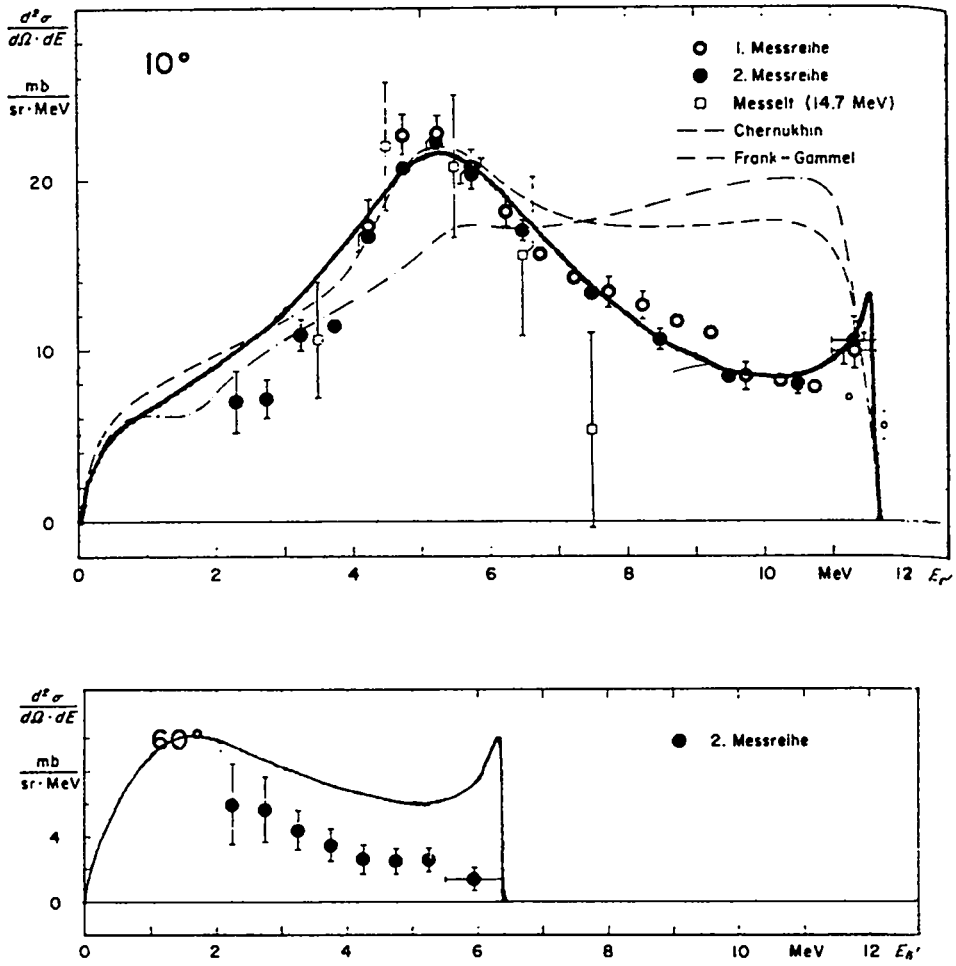

Fig. 1.

Resonance model calculations (solid curves) compared to measured n+d neutron spectra at θ_{LAB} = 10 and 60 degrees for 14.1-MeV incident neutrons. The dashed and dot-dashed curves at 10 degrees are other calculations, and the circles and squares are measured values.

angles. The calculations are normalized to the data at forward angles, and there the agreement is good. At back angles, the calculated spectra overpredict the data considerably.

Because the wavefunction is antisymmetric under exchange of the two neutrons, the singlet n-p resonance (the "virtual" deuteron), which is essentially all that is in the calculation, causes both the final-state-interaction peak at the upper end of the spectra and the broad central maximum at the forward angles. Also, the interference term has an important effect on the spectral shapes in this case. Thus, n+d spectra appear to be good examples of broad structure coming from a kinematically broadened resonance, rather than from three-body-phase space contributions.

Some of the assumptions and approximations that remain in the model are being relaxed in an effort to improve the calculated spectra at back angles.

B. Analysis of n+ ^{169}Tm Reactions [P. G. Young, E. D. Arthur; C. Philis, P. Nagel, and M. Collin (Bruyères-le-Châtel)]

As part of a program to produce reliable nuclear data calculations for several Tm isotopes, a theoretical analysis of experimental data for n + ^{169}Tm reactions is in progress. In a previous progress report, Arthur[2] described a deformed optical model analysis that led to a set of parameters (referred to as Set No. 1 here) in reasonable agreement with ^{165}Ho total cross sections between 0.05 and 20 MeV, s- and p-wave neutron strength functions for ^{165}Ho, elastic angular distributions, and 16-MeV proton scattering data to the ^{165}Ho ground and first excited states. These parameters were applied to ^{169}Tm through use of an isospin term in the real and imaginary well depths, along with adjustment of the β_2 and β_4 deformation parameters based on available systematics in this mass region.

To test the parameters from this analysis, calculations were made of the ^{169}Tm total cross section and the ^{169}Tm(n,γ), (n,2n), and (n,3n) reactions at neutron energies where data were available. The computer codes used were ECIS[3] for the deformed optical model calculations, COMNUC[4] for the (n,γ) calculations, and GNASH[5] for the (n,2n) and (n,3n) calculations. At most energies the agreement with experiment was quite satisfactory; however, the calculated total cross section was found to be systematically ~4% lower than experiment at energies between 8 and 12 MeV. Because of this disagreement, an effort was made to further optimize the initial set of parameters by comparing trial and

error deformed optical model calculations with the ^{169}Tm total cross section and s-wave strength function, as well as the ^{165}Ho data mentioned earlier.

The results of this analysis (referred to as Set No. 2) are compared to the original analysis (Set No. 1) in the table and figures that follow. Table I lists the two sets of deformed optical model parameters that were obtained. Note that the only differences in the two parameter sets are in the β_2 deformation, the radius parameter, and the surface-derivative imaginary potential. The calculated s- and p-wave neutron strength functions are compared with experiment and systematics in Table II. Calculations with the two parameter sets are compared to ^{169}Tm total cross-section measurements in Fig. 2, to ^{169}Tm(n,γ) measurements in Fig. 3, to ^{169}Tm(n,2n) measurements in Fig. 4, to ^{169}Tm(n,3n) measurements in Fig. 5, and to a ^{165}Ho(n,n) elastic angular distribution measurement at 11 MeV in Fig. 6. In all cases,the same values for $2\pi\langle\Gamma_\gamma\rangle/\langle D\rangle$ (= 0.0795) and for the preequilibrium parameters (g_0 = A/13, k = 130 MeV^3) were used in the calculations with the two deformed optical model parameterizations. To summarize the results, there appears to be good overall agreement with experiment using both sets of parameters. There is some preference for Set 2, however, on the basis of the total cross section, s-wave strength function, and (n,2n) cross-section comparisons.

TABLE I

n + ^{169}Tm OPTICAL MODEL PARAMETERS[a]

A. Common Parameters

$V_R = 46.87 - 0.25\ E_c$ a = 0.63

$W_{SD} = 3.6 + 0.6\ E_c$ [$E_c \leq 6.5$ MeV] a = 0.48

$W_V = 0$ [$E_c \leq 9$ MeV]
$= -1.8 + 0.2\ E_c$ [$E_c > 9$ MeV] a = 0.63

$W_{SO} = 6.0$ a = 0.63

$\beta_4 = -0.01$

TABLE I (Cont)

B. Parameter Differences

Set #1: $\beta_2 = 0.288$

$r_0 = 1.26$

$W_{SD} = 7.5 - 0.1\ (E_c - 6.5)$ $[E_c > 6.5$ MeV$]$

Set #2: $\beta_2 = 0.31$

$r_0 = 1.27$

$W_{SD} = 7.2 - 0.03\ (E_c - 6.0)$ $[E_c > 6.0$ MeV$]$

[a]All depths given in MeV, geometrical parameters in fm.

TABLE II

SUMMARY OF n + ^{169}Tm S_0, S_1, R' RESULTS

	Exp.	Set #1	Set # 2
S_0 ($\times 10^{-4}$)	1.5 ± 0.2	1.97	1.65
S_1 ($\times 10^{-4}$)	0.5 - 1.5[a]	2.38	3.60
R' (f)	7.7 ± 0.5	7.77	7.55

[a]Inferred from systematics

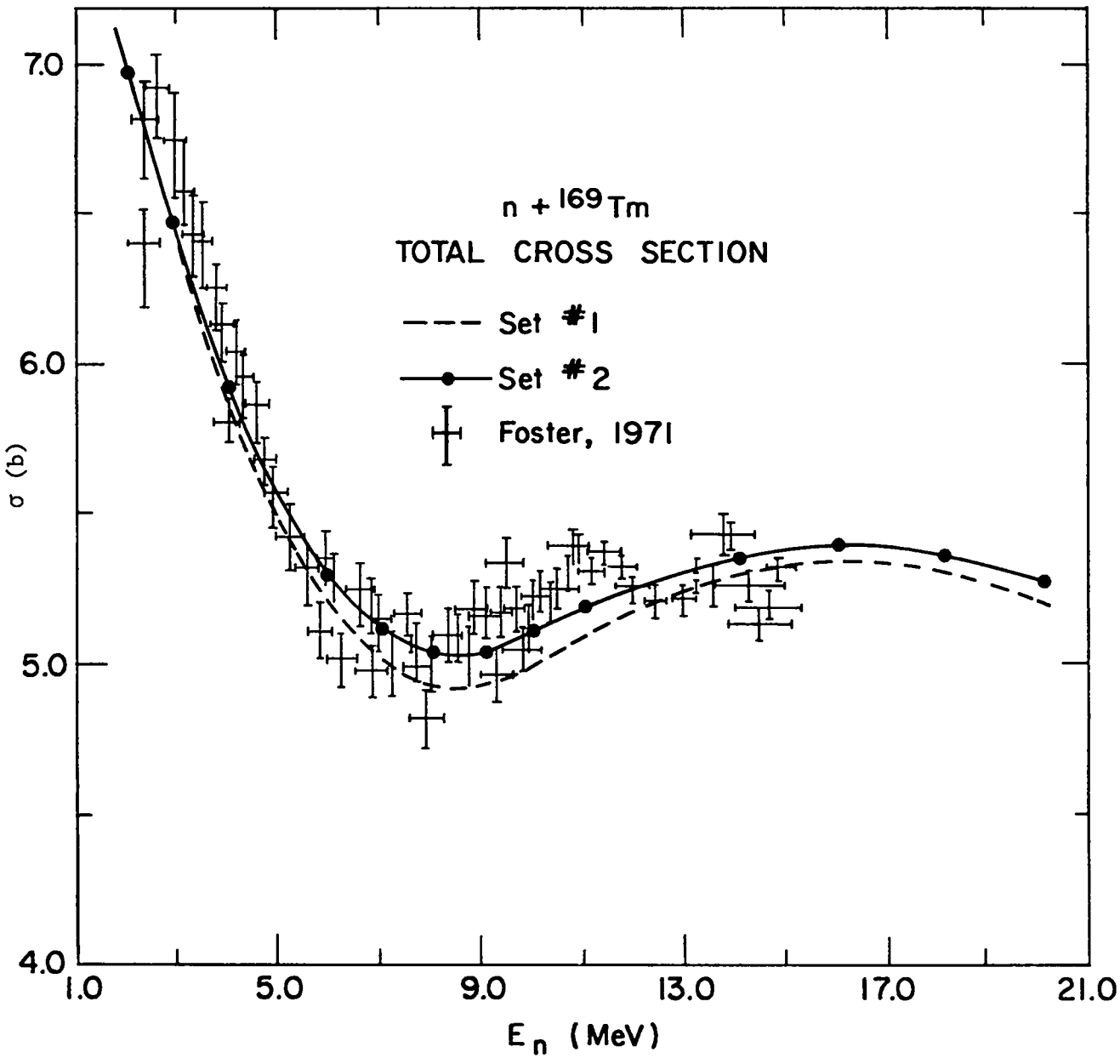

Fig. 2.

Comparison of calculated and measured values of the n + ^{169}Tm total cross section.

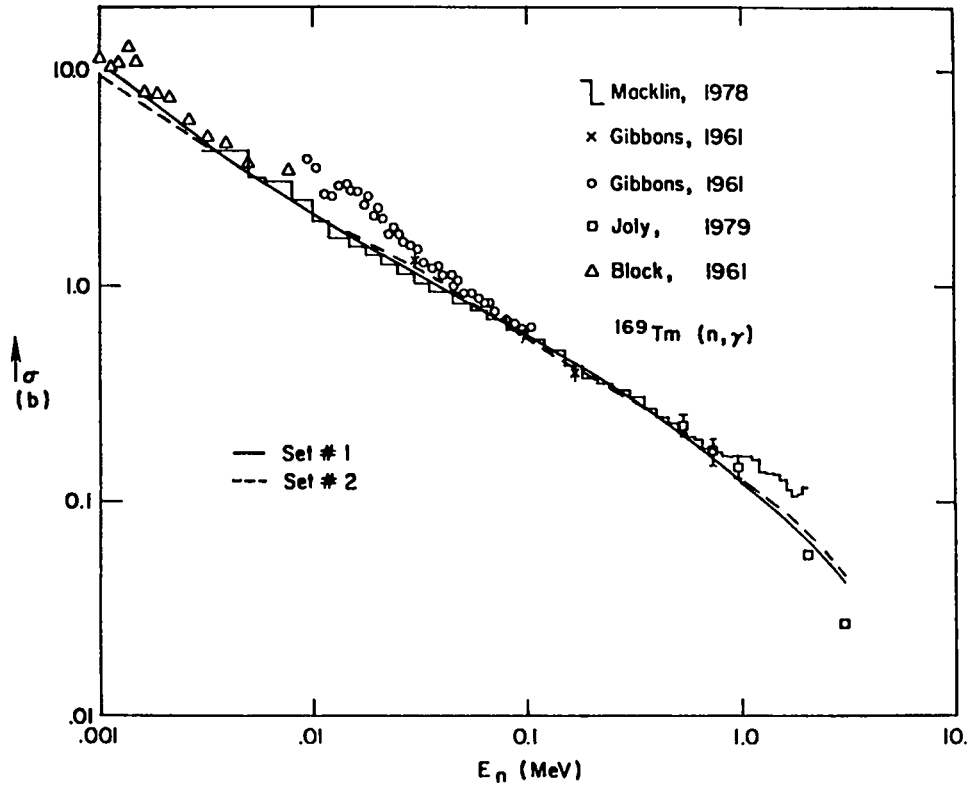

Fig. 3.

Calculated values of the $^{169}Tm(n,\gamma)$ cross section compared to several experimental results.

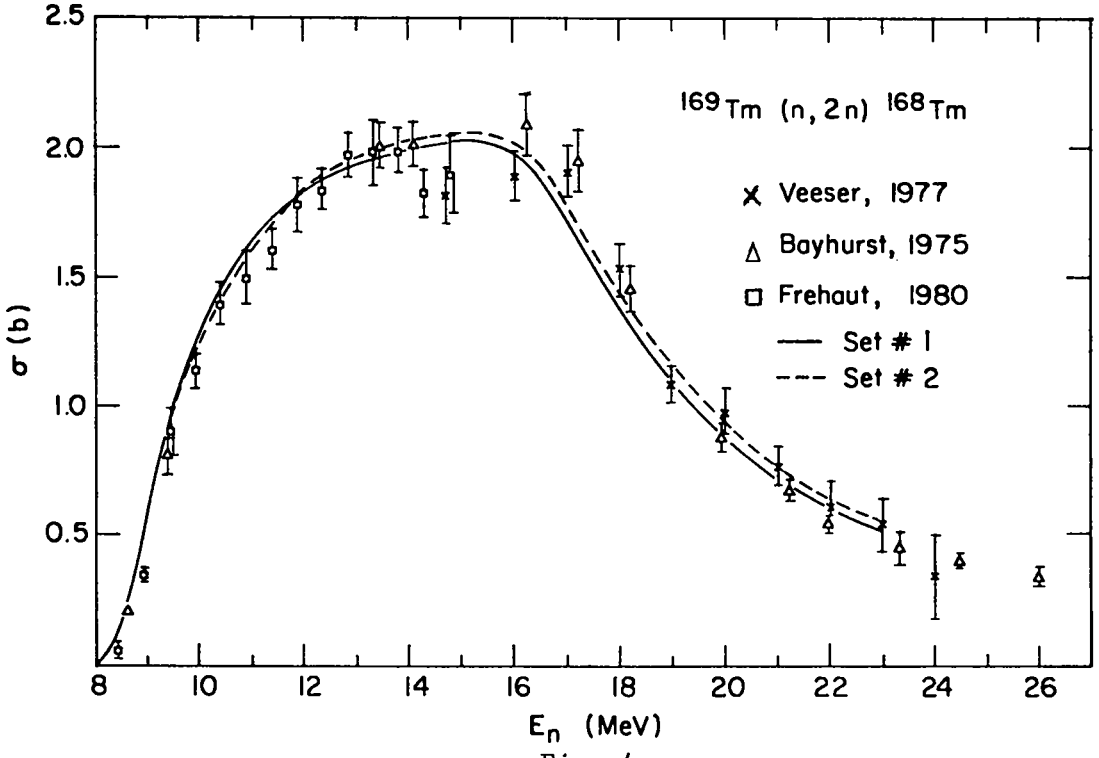

Fig. 4.

Calculated and measured ^{169}Tm (n,2n) cross section.

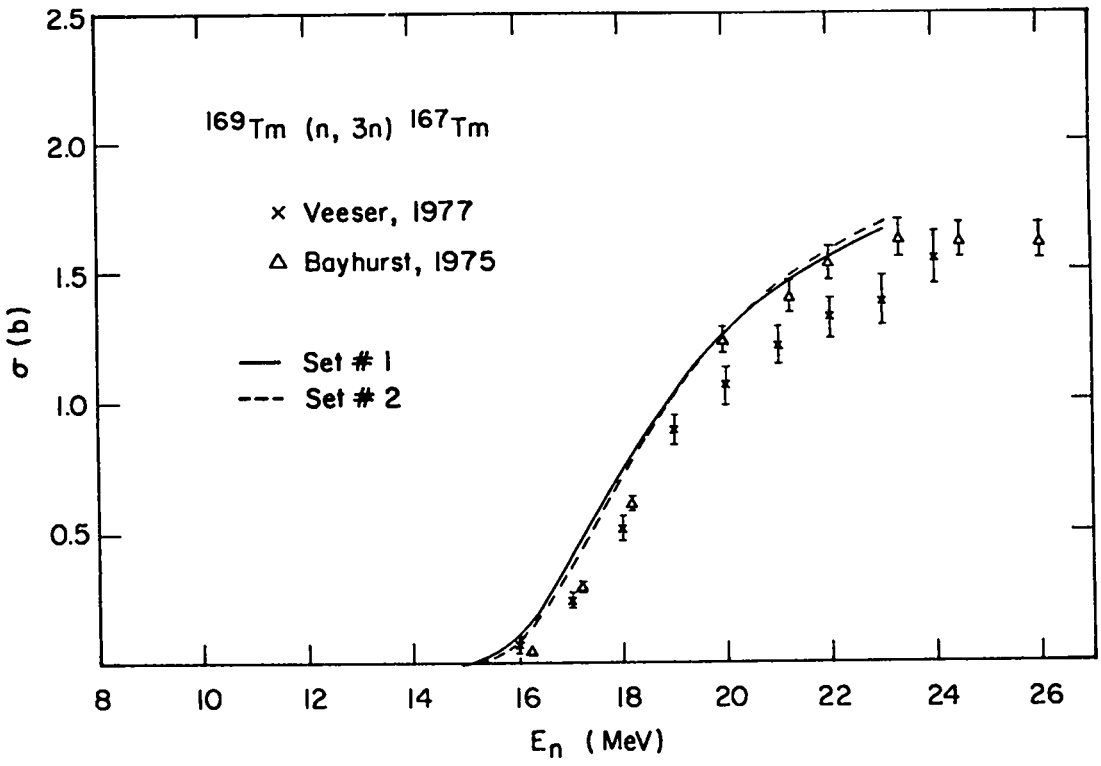

Fig. 5.
Calculated and measured ^{169}Tm(n,3n) cross section.

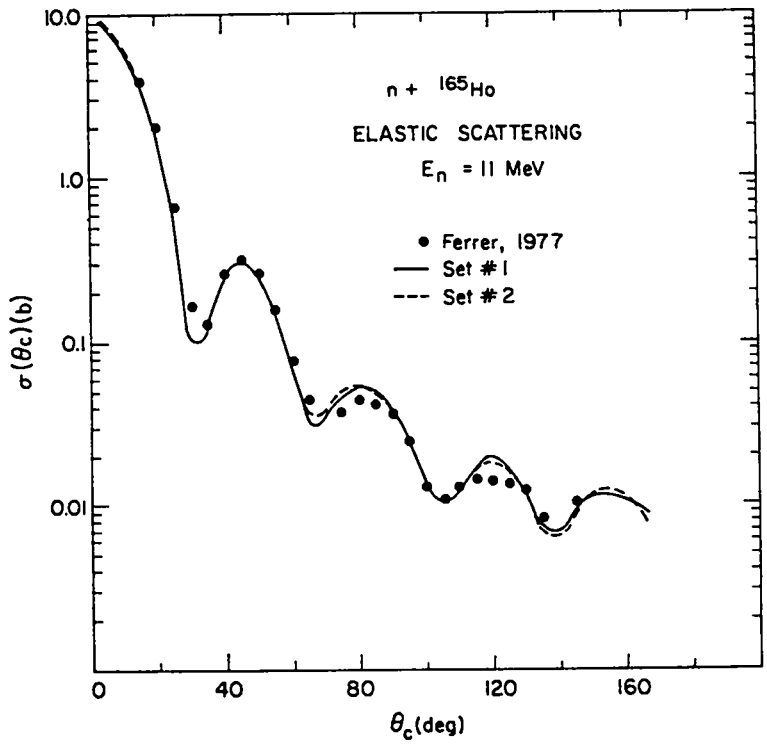

Fig. 6.
Comparison of calculated ^{165}Ho (n,n) elastic angular distributions with experimental measurements.

C. Improvements of the Fission Channel in COMNUC (E. D. Arthur)

The fission channel representation in the Hauser-Feshbach statistical model code COMNUC[6] has been improved to incorporate more realistic methods for determination of fission barrier penetrabilities, as well as increased flexibility in the phenomenological description of transition-state densities at the barriers.

The previous version of COMNUC in use at Los Alamos and Livermore for many years employed a Hill-Wheeler[7] inverted parabola to represent the fission barrier, which results in a fission penetrability of the form

$$P_f = (1 + \exp (2\pi/\hbar\omega (B_f - E))^{-1} \quad (1)$$

where B_f and $\hbar\omega$ are the barrier height and curvature, respectively. Low-lying transition states could be specified explicitly, but at higher energies above the barrier, the continuum of such states was represented by a Gilbert-Cameron[8] level-density expression having essentially the same parameters as for the ground-state deformation. A factor could be applied to the Fermi-gas parameter $\underline{a}$ to allow compression of the level density at the barrier.

The presence of fission isomers, along with structure in fission probabilities obtained from direct-reaction studies[9,10] and structure in (n,f) cross sections, has lead to the formulation of a double-humped barrier model to explain such phenomena. In the new version of COMNUC, we have followed the technique of Back et al.[9,10] in which the one-dimensional double-humped barrier shown in Fig. 7 is approximated, as in Fig. 8, by the two parabolic sections joined smoothly at points a and b. With this representation, six parameters are needed to specify the barriers, their heights E_A and E_B, and curvatures $\hbar\omega_A$, $\hbar\omega_B$ along with the height and curvature of the second minimum. An imaginary potential is introduced into the second well to simulate damping of the Class II vibrational structure into the Class II compound states. The resulting penetrability calculated from such a double-humped model is not a smoothly increasing function of energy as would be obtained from Eq. (1), but instead includes structure occurring at energies corresponding to that of vibrational Class II states, as shown in Fig. 9.

Where two such coupled oscillators represent the fission barrier, the total fission transmission coefficient is obtained from the following schematic expression[9]

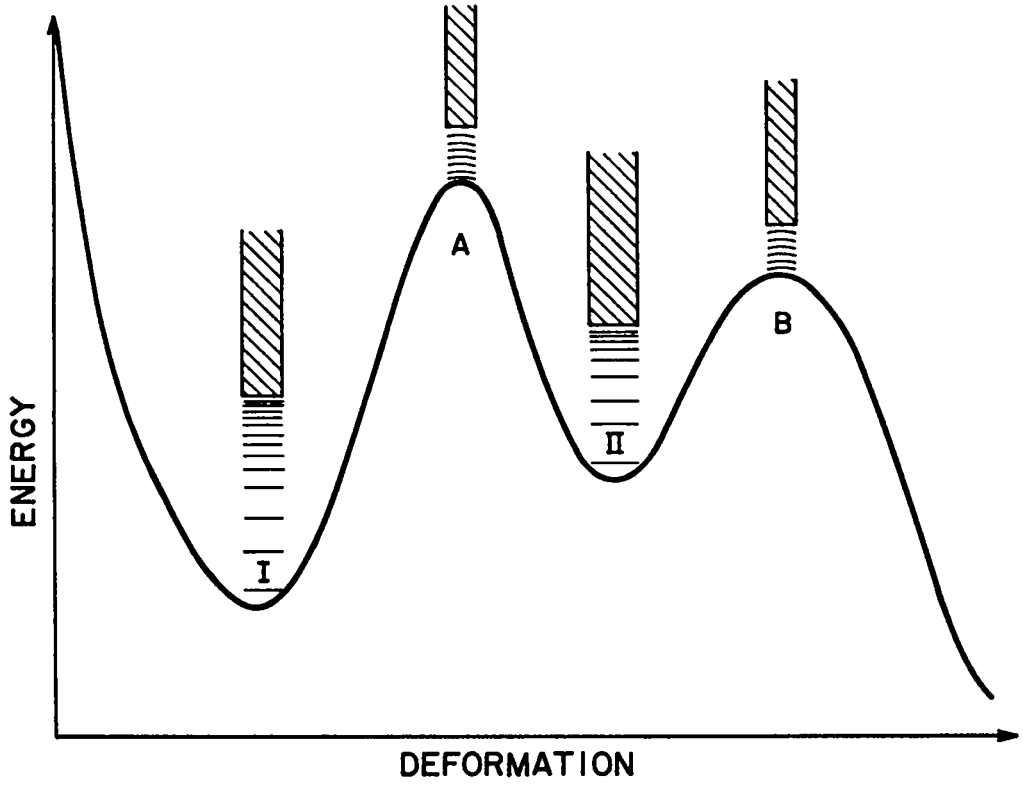

Fig. 7.
A one-dimensional representation of the double-humped fission barrier. Class I and II states occur in the first and second well, respectively, while above the saddle points at A and B, a spectrum of discrete barrier transition states occurs followed at higher energies by a continuum of such states.

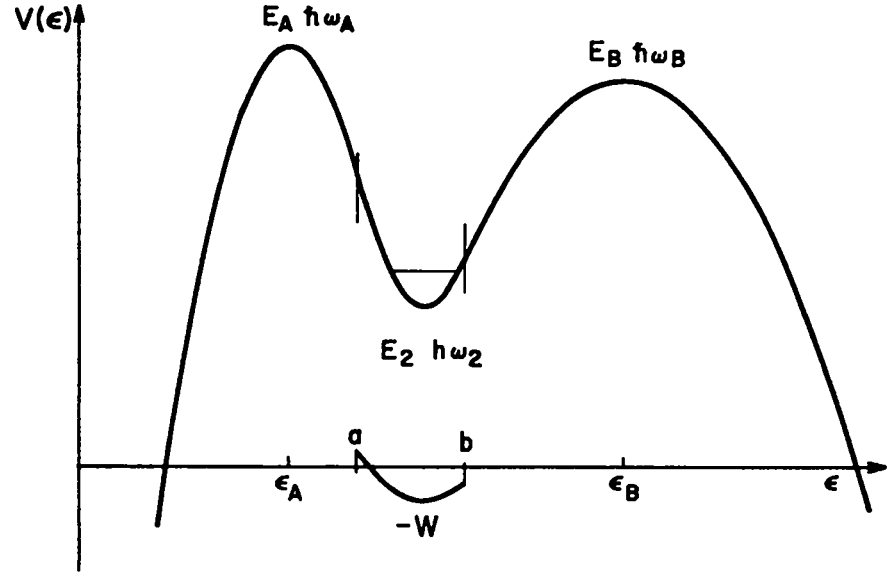

Fig. 8.
The approximation to the double-humped barrier shown in Fig. 7, which is used to calculate fission penetrabilities. Three parabolas are joined smoothly at points a and b. Also shown is the negative imaginary potential provided to permit damping of the Class II states in the second well.

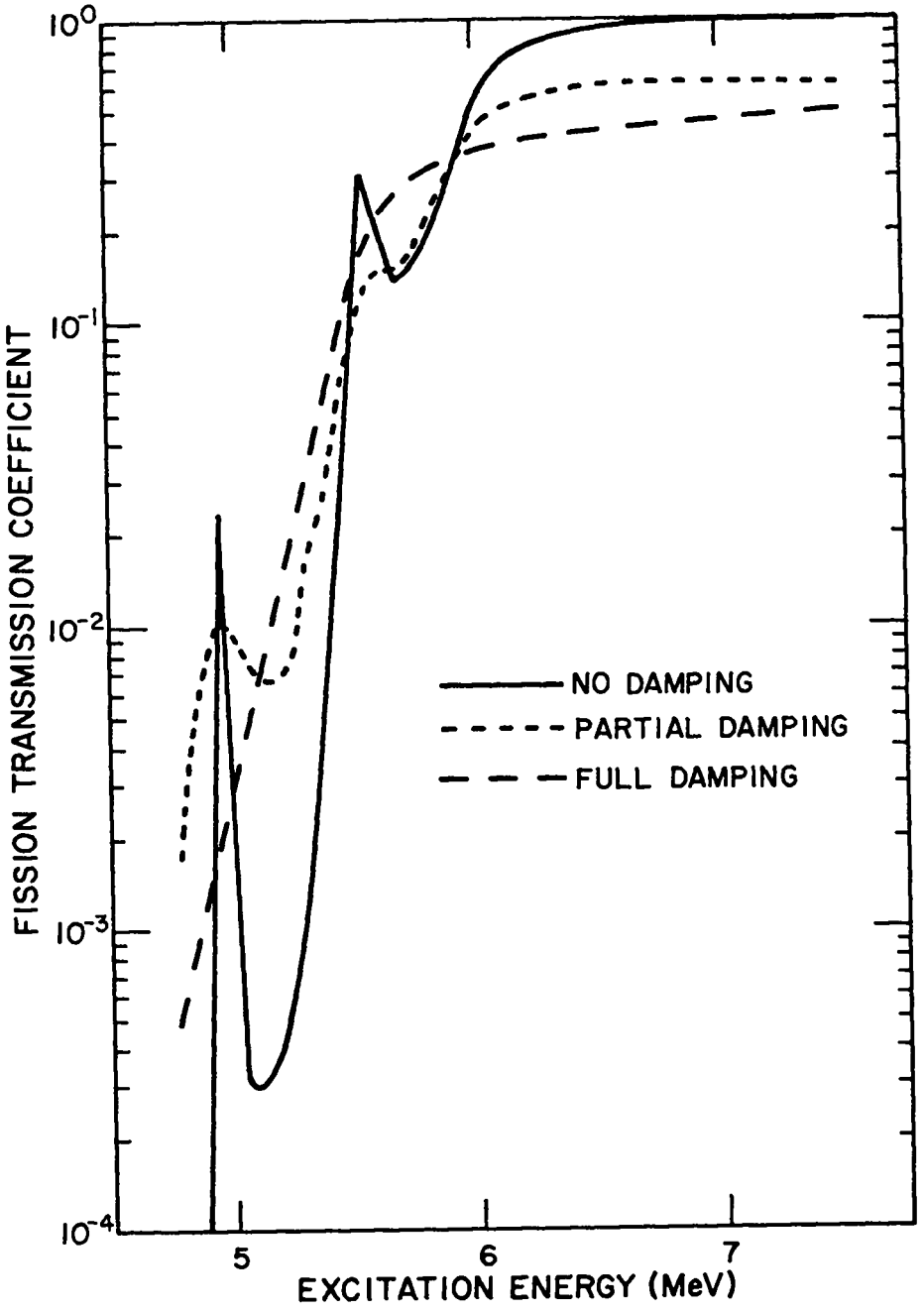

Fig. 9.

Variation of the total fission transmission coefficient calculated for the case of no damping (W = 0), moderate damping, and full damping.

$$T_F = N_D + \frac{N_A P_B}{P_A + P_B} F_{II} \tag{2}$$

Here N_D represents the portion of the directly transmitted flux summed over transition states (and/or integrated over the continuum of such states). The absorbed flux summed over transition states at barrier A (or integrated over the continuum) is represented by N_A. The quantities P_A and P_B consist of the penetrabilities obtained from the Hill-Wheeler expression of Eq. (1) again summed or integrated over discrete and continuum transition states. The factor F_{II} describes the strong fluctuations in the fission width that occur near Class II states where strong coupling produces enhanced absorption. Likewise, suppression occurs between such resonances. As shown in Eq. (2), such fluctuations apply only to the flux absorbed in the second well at energies below the barrier where Class II state widths are much smaller than their spacing. The computation of this factor is based on the results of Lynn and Back[11] in which a spectrum of equidistant Class II resonances of Lorentzian shape and equal strength is assumed. In addition to these fluctuations, the width fluctuation factor normally associated with the Hauser-Feshbach statistical expression must be applied assuming a normal distribution having a width ν given by the number of open fission channels.

At excitation energies high above the barrier or for compound systems where the barrier heights lie much lower than the neutron separation energy, the damping of the Class II states increases, so that in Eq. (2) $N_D \to 0$ and $N_{ABS} \to P_A$. Thus, in the limit of strong damping, the expression for the fission transmission coefficient reduces to that for two uncoupled oscillators

$$T_F = \frac{P_A P_B}{P_A + P_B} F_{II} \tag{3}$$

where

$$P_{A,B} = \sum_i (1 + \exp(2\pi/\hbar\omega_{A,B}(E_{A,B} - E_i))^{-1} + \int \rho^{A,B}(1 + \exp 2\pi/\hbar\omega_{A,B}(E_{A,B} - \varepsilon))^{-1} \, d\varepsilon \, . \tag{4}$$

To reduce computation times in strongly damped cases, expression (3) is used to calculate the fission width.

Important to the calculation of the fission transmission coefficient using expressions (2) or (3) is an adequate representation of the transition states lying above the barrier. Thus, up to 50 such states can be supplied to the code. Above the last discrete transition state a phenomenological level density expression[8] consisting of constant-temperature and Fermi-gas forms is used. It has been shown by Gavron et al.[12] in the analysis of Γ_n/Γ_f ratios and by Bjørnholm et al.[13] from theoretical arguments that the level density at the saddle points A or B will be enhanced over that assumed for the ground-state deformation. The maximum enhancement occurs for cases having no symmetry, a situation that occurs for the inner barrier of nuclides having Z >93. Other symmetries, such as reflection or nonaxial symmetry, reduce the enhancement over this extreme case. The second barrier is generally considered to be mass asymmetric (no reflection symmetry) with a resulting enhancement of two, although increased enhancements are possible. Thus, in the new COMNUC version, an effort has been made to incorporate the general principles governing such enhancements while maintaining the flexibility needed to reproduce measured (n,f) cross sections. The level density used at barrier A or B is first calculated using the basic Gilbert-Cameron phenomenological model. It is then multiplied directly by an enhancement factor provided separately for barrier A or B. Since these factors are proportional to the spin cutoff parameter σ (the maximum for cases having no symmetry being $\sigma\sqrt{8\pi}$), the energy dependence is taken to be proportional to $U^{\frac{1}{4}}$ since $\sigma^2 = 0.088\ A^{2/3}\ \sqrt{aU}$ in the Gilbert-Cameron model. From preliminary calculations on $^{235,238}U$ and $^{239,242}Pu$, the use of this approach has resulted in good fits to measured (n,f) cross sections with enhancement factors that agree with those obtained in more microscopic calculations.[14]

In addition to these fission channel improvements, COMNUC has been upgraded to include inelastic scattering from up to 40 target nucleus levels. Also the constant temperature parameters are now adjusted automatically, based on information provided concerning the cumulative number of levels occurring at a given excitation energy.

D. Average Neutronic Properties of "Prompt" Fission Products (D. G. Foster, Jr.)

At the request of users of the data sets generated from our "prompt" fission-product evaluation,[15,16] the energy range has been extended below 1 keV, so that it now covers the full ENDF/B range of 10^{-5} eV to 20 MeV. The sub-keV range is assumed to have a constant elastic cross section equal to the value calculated at 1 keV. The slow-neutron cross section is taken to be the cross section of the ground state of ^{135}Xe multiplied by its prompt yield for fast fission of ^{235}U or ^{239}Pu, respectively. We assume the ^{135}Xe cross section behaves as 1/v below thermal, rises linearly on a log-log scale from thermal to its maximum near 0.1 eV, and drops linearly on a log-log scale above the maximum with the same slope as the measured total cross section. Because the calculated capture cross section of the fission fragments just above 1 keV is also a straight line on a log-log plot, we follow the ^{135}Xe cross section down until it intersects the extrapolated fission-fragment cross section near 1 eV, and transfer there to the extrapolated line. The result is illustrated in Fig. 10. The photon-production cross section shown in the figure assumes that the multiplicity is constant below 1 keV.

Because the yield of ground-state ^{135}Xe is about fivefold greater for fast fission of ^{239}Pu than for ^{235}U, our assumed slow-neutron cross sections exhibit the same factor-of-five difference. The COMNUC and GNASH calculations indicate that the capture cross section of ^{239}Pu fragments is about a factor-of-two greater than for ^{235}Pu fragments above 1 keV. This higher energy difference does not appear, on closer examination, to be the chance effect of one anomalous target nuclide in our ten-nuclide averages. On the contrary, it appears to be a true systematic effect of the greater average mass of the plutonium fragments.

Figures 11 and 12 illustrate the neutron and photon spectra calculated in the course of this program. There do not appear to be pronounced differences between the spectra for the two targets, other than the expected effects of different thresholds and of discrete transitions at low bombarding energies.

The final report on the program will be issued shortly as a Los Alamos National Laboratory report LA-9168-MS.

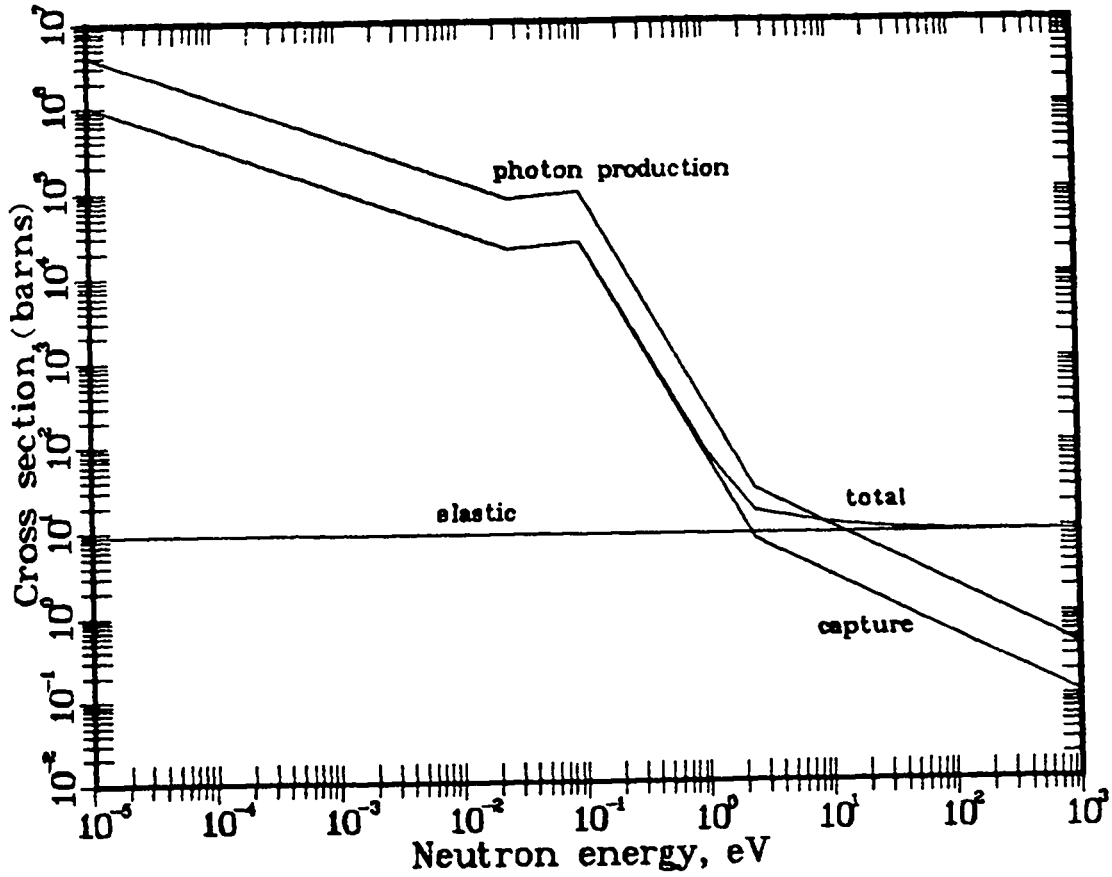

Fig. 10.

Estimated cross sections of ^{239}Pu fission fragments below 1 keV.

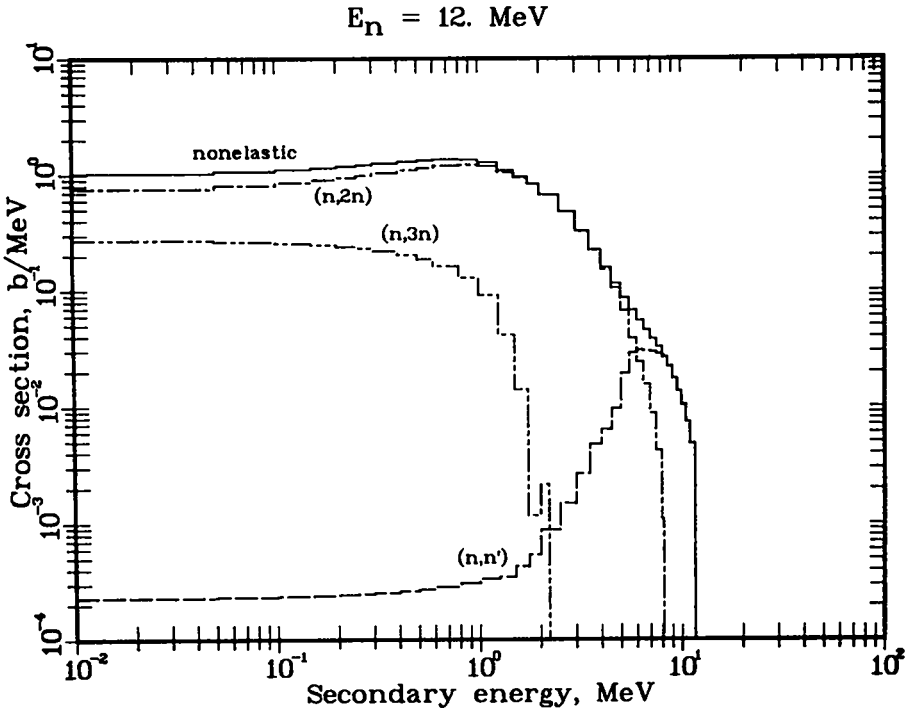

Fig. 11.

Neutron spectra from bombardment of ^{235}U fast-fission fragments with 12-MeV neutrons.

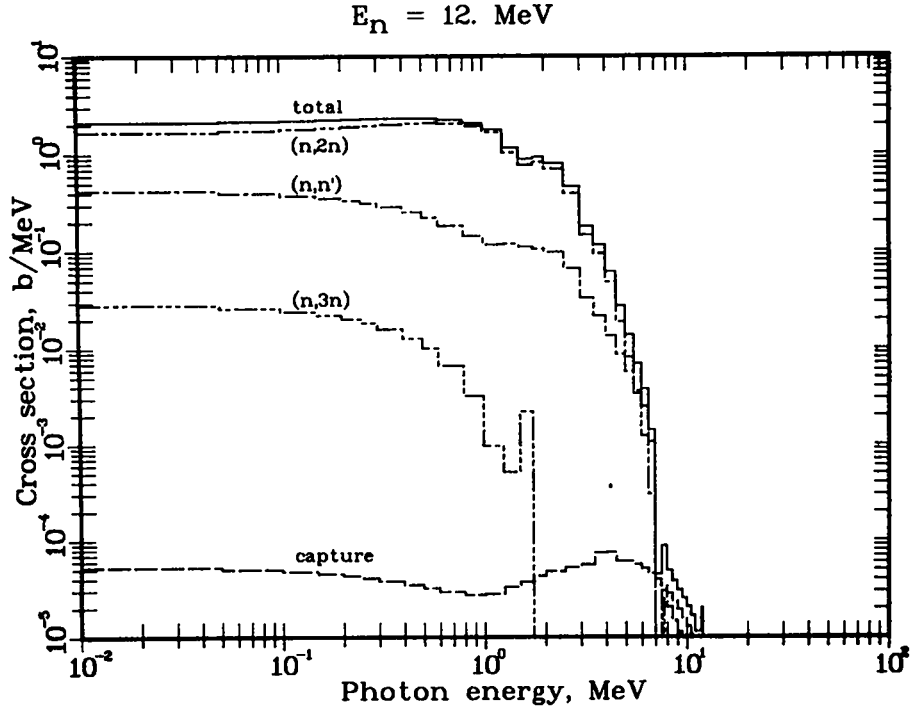

Fig. 12.

Photon spectra from bombardment of ^{235}U fast-fission fragments with 12-MeV neutrons.

E. New Calculation of Prompt Fission Neutron Spectrum N(E) and Average Prompt Neutron Multiplicity $\bar{\nu}_p$ [D. G. Madland and J. R. Nix (T-9)]

An extensive manuscript summarizing this work has been completed and submitted to Nuclear Science and Engineering for publication. The work has shown that N(E) and $\bar{\nu}_p$ can be accurately predicted to within a few per cent, given certain well-measured fission-related quantities, and otherwise to within perhaps 5-10% when these same quantities are instead calculated. We have found that it is necessary to take into account the facts that fission fragments are formed with a distribution of excitation energy and that the inverse process of compound-nucleus formation is energy dependent. We have learned that it is essential to calculate N(E) and $\bar{\nu}_p$ simultaneously to ensure accurate results. We have shown that the dependence of $\bar{\nu}_p$ on incident neutron energy is not strictly linear, as is almost always assumed, but that the dependence is somewhat weaker than a linear assumption. Using a method to extract multiple-chance fission probabilities from total fission-cross-section measurements, we have determined that at high excitation of the fissioning nucleus, multiple-chance fission processes must be included in the calculation of N(E) but that they have only a slight effect on $\bar{\nu}_p$. Finally, we have developed a method by which our exact calculations involving numerical integrations can be simulated with closed-form expressions, which simplifies enormously the application of our approach to practical problems.

The calculations to date have been performed for a single choice of the nuclear level-density parameter and without the use of any further adjustable parameters. For the purposes of nuclear evaluation in those circumstances where experimental prompt fission neutron spectra exist, the nuclear level-density parameters could be adjusted to optimally reproduce the experimental spectra for the nucleus in question. However, a large change in the nuclear level-density parameter will affect the value of the calculated $\bar{\nu}_p$. Thus, care must be exercised in such an approach.

Certain additional studies are suggested by our work. These include an improved calculation of the average fission energy release $\langle E_r \rangle$, the use of a more realistic form of the fission-fragment nuclear temperature distribution P(T) than the triangular form currently used, and the relaxation of the assumption that, on the average, equal numbers of neutrons are emitted by the light and heavy fragment groups.

F. Prompt Fission Neutron Spectrum Matrix for ^{235}U (D. G. Madland)

A prompt fission neutron spectrum matrix $N(E,E_n)$ has been calculated to provide a chi matrix for use in applied physics considerations. The matrix has been calculated using the theory of Refs. 17-23. The case calculated is that of the neutron-induced fission of ^{235}U for incident neutron energies E_n, ranging from 0 MeV to 15 MeV, and for secondary neutron energies E, ranging from 10^{-5} MeV to 50 MeV. The effects of, and competition between, first-chance, second-chance, and third-chance fission are included in the calculation. The matrix is defined such that

$$\int_0^\infty N(N,E_n)dE = 1$$

for each value of E_n. The units of E and $N(E,E_n)$ are MeV and MeV^{-1}, respectively. [For Los Alamos users, the matrix $N(E,E_n)$ is available on the CFS as the green file U5MTRX, which is accessed with the command

MASS GET DIR=/081380/WCODES U5MTRX.

The file consists of 16 blocks of $E,N(E,E_n)$ pairs in FORMAT(5X,1P6E15.6), each block containing 581 pairs in 194 lines. The blocks are ordered in increasing values of E_n in 1 MeV steps beginning with 0 MeV and ending with 15 MeV. In addition, the file U5MTCK, having the identical format, but corresponding to E_n values of 0.5, 1.5, 2.5, and 3.5 MeV, is available from the same directory so that the user of U5MTRX can test various interpolation schemes and/or increase the density of points at low incident neutron energy.]

Three-dimensional plots of the prompt fission neutron spectrum matrix are shown in Figs. 13 and 14. In Fig. 13 an absolute plot of $N(E,E_n)$ vs E and E_n is shown for the ranges 10 keV $\leq$ E $\leq$ 15 MeV and 0 MeV $\leq E_n \leq$ 15 MeV. In Fig. 14 a ratio plot of $R(E,E_n) = N(E,E_n)/N(E,0)$ vs E and E_n is shown for the ranges 10 keV $\leq$ E $\leq$ 20 MeV and 1 MeV $\leq E_n \leq$ 15 MeV. These figures clearly illustrate the dependence of the matrix upon the incident neutron energy E_n, particularly in the tail region corresponding to high secondary neutron energy E where the matrix generally becomes harder with increasing E_n. The observed modulation of this behavior is caused by multiple-chance fission effects. Specifically, as E_n increases beyond about 6 MeV, the tail region softens somewhat because part of the nuclear excitation energy is dissipated by the emission of a neutron prior to fission. This softening is observed again as E_n increases beyond about 13 MeV where part of the excitation energy is dissipated by the emission of two neutrons prior to fission.

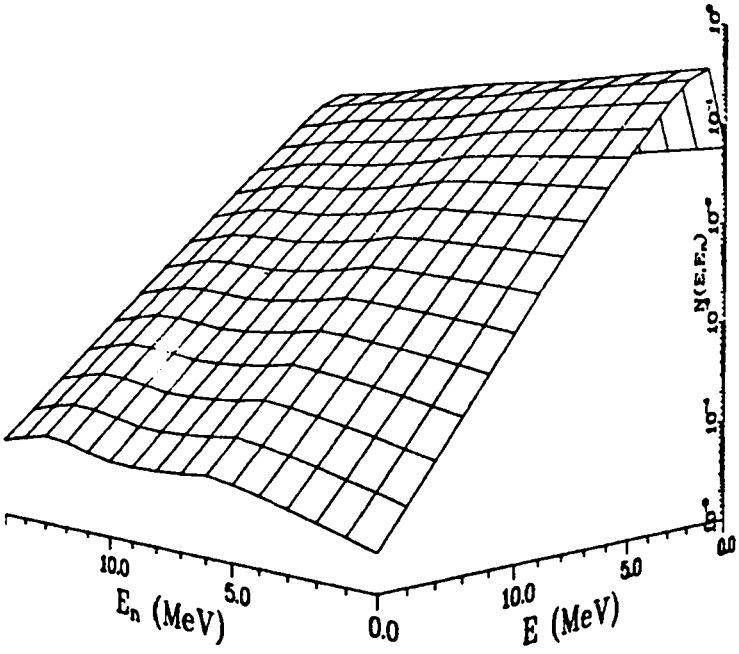

Fig. 13.

Prompt fission neutron spectrum matrix $N(E,E_n)$ for the neutron-induced fission of ^{235}U as a function of the incident neutron energy E_n and the secondary or emitted neutron energy E. The matrix is in the laboratory system. The calculation is performed using the formalism detailed in Refs. 17-23. In particular, energy-dependent cross sections are used, which are determined from the optical-model potential of Ref. 26.

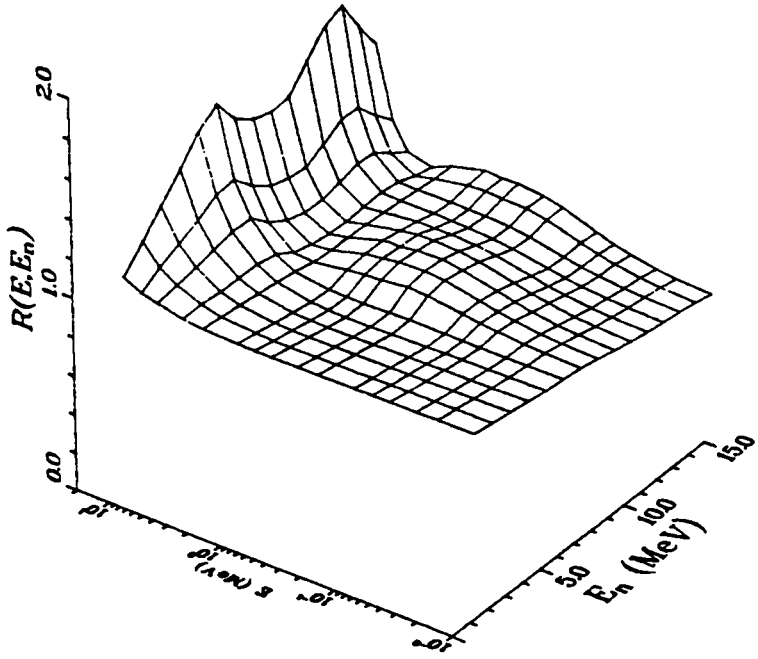

Fig. 14.

Prompt fission neutron spectrum ratio matrix $R(E,E_n) = N(E,E_n)/N(E,0)$ obtained by forming the ratio of each spectrum of Fig. 13 to the thermal spectrum ($E_n = 0$) of Fig. 13. The unit line corresponding to the thermal spectrum divided by itself is not shown in the figure.

Two comparisons of the new calculation with experimental data are shown in Figs. 15 and 16. In Fig. 15 the calculated prompt fission neutron spectrum shown by the solid curve is compared to experiment[24] for 0.53-MeV incident neutrons and for secondary neutrons ranging in energy from about 0.5 MeV to 14.5 MeV. Thus, in terms of the matrix, the N(E,0.53) cut is compared with experiment in this figure. In Fig. 16 the calculated average prompt neutron multiplicity $\bar{\nu}_p(E_n)$ shown by the solid curve is compared to experiment[25] for incident neutron energies ranging from thermal energy to about 15 MeV. Note that in all of our calculations the optical-model potential of Ref. 26 is used. The relationship to the matrix is that for each value of E_n certain quantities required for the calculation of $\bar{\nu}_p(E_n)$ are also required for the calculation of $N(E,E_n)$. Thus, agreement between calculated and experimental values of $\bar{\nu}_p(E_n)$ lends a measure of confidence to the calculated $N(E,E_n)$.

In future work we will calculate the prompt fission neutron spectrum matrices for the neutron-induced fission of ^{238}U and ^{239}Pu. We expect to begin these calculations following early results and comments from the users of the present matrix for ^{235}U.

G. Calculation of Excited-State Cross Sections for Actinide Nuclei (D. G. Madland)

A test calculation has been performed using the excited-state coupled-channel code JUPXST.[27] The test calculation consists in coupling the first three members of the ground-state, K = 0, rotational band in the target nucleus ^{238}U for incident neutrons ranging in energy from 10 keV to 10 MeV. Two cases have been calculated for comparison, namely, that of the target nucleus in its ground state (0^+_o, 0.00 MeV), and that of the target nucleus in its first excited state (2^+_o, 0.045 MeV).

The two cases are calculated assuming an axially symmetric rotor description of the target nucleus in the collective-model approximation. Quadrupole and hexadecapole deformations are included in the collective-radius expansions used in the form factors of the interaction potential which, as a consequence, is deformed. We approximate the interaction potential by a deformed complex phenomenological optical-model potential and perform the calculations using two such potentials derived on the basis of three-state coupling in the symmetric-rotor description. These potentials are the actinide coupled-channel potential of Madland and Young[28] and the ^{238}U coupled-channel potential of Lagrange.[29]

Fig. 15.
Prompt fission neutron spectrum in the laboratory system for the fission of ^{235}U induced by 0.53-MeV neutrons. The curve gives the spectrum obtained with the new calculation using energy-dependent cross sections $\sigma_c(\epsilon)$ from the optical model potential of Ref. 26. The experimental data are from Ref. 24.

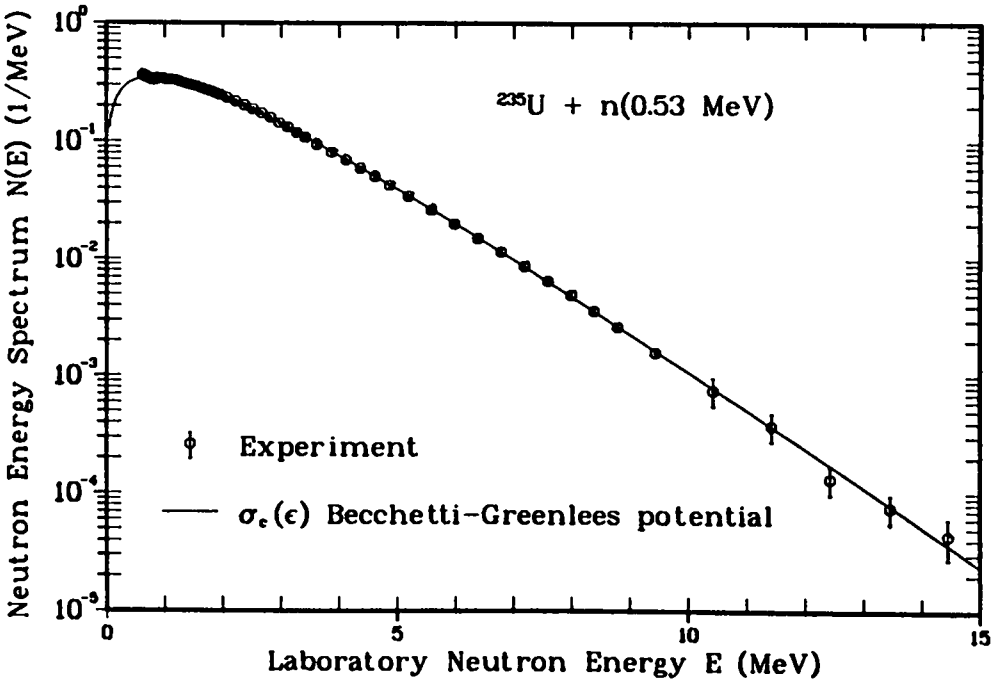

Fig. 16.
Average prompt neutron multiplicity as a function of the incident neutron energy for the neutron-induced fission of ^{235}U. The curve gives the multiplicity obtained with the new calculation including first-chance, second-chance, and third-chance fission effects. The calculation uses energy-dependent cross sections $\sigma_c(\epsilon)$ obtained from the optical model potential of Ref. 26. The experimental data are from a number of independent measurements (see Ref. 25). Note the suppressed zero of the vertical scale.

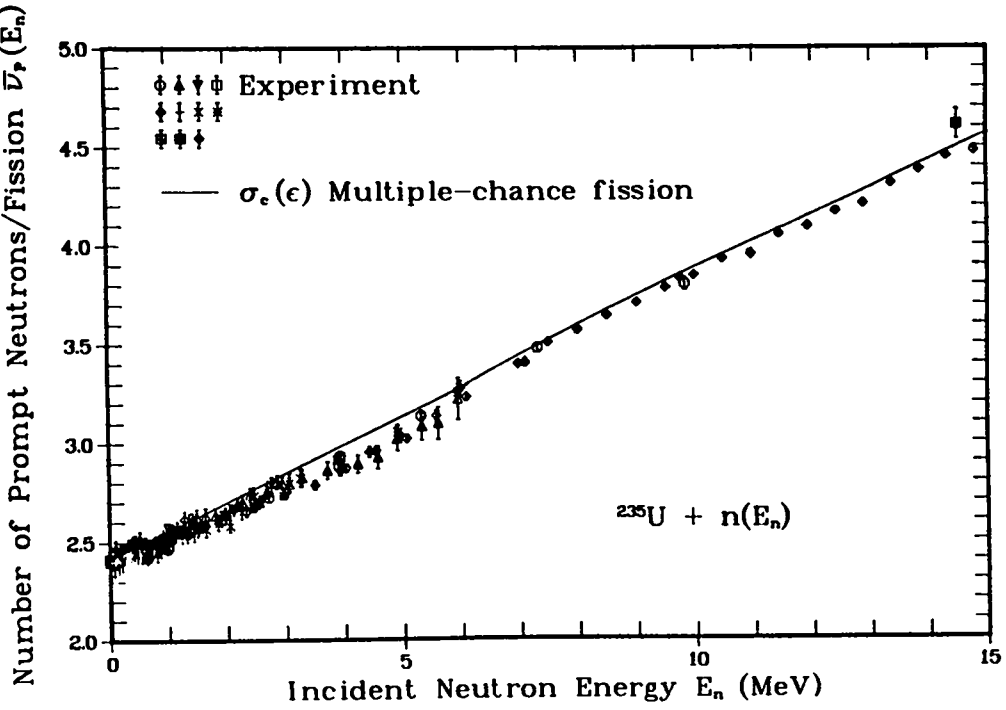

Other details of the calculations are that the expansion order of the interaction potential used in JUPXST is $\lambda = 4$ (Legendre polynomial P_4), that the matching radius R_m is given by the maximum value of $r_o A^{1/3} + 12a$ from the set of form-factor geometries considered, and that the maximum value of the projectile orbital angular momentum ℓ_{max} for a given projectile wave number k is given by

$$\ell_{MAX} = 2kR + I_{max}$$

where $R = r_o A^{1/3}$ and I_{max} is the maximum spin occurring in the set of coupled states ($I_{max} = 4$ in the cases considered here). The expressions given for R_m and ℓ_{max} have been determined in a series of convergence test calculations.

Our results are shown in Figs. 17-21 as differences between excited-state and ground-state calculations for the two potentials considered, namely, the potential of Ref. 28, designated as the Harwell potential in the figures, and the potential of Ref. 29, designated as the B-III potential in the figures. Differences between excited-state and ground-state calculations are shown for the total, elastic, reaction, direct-inelastic, and compound-nucleus cross sections in Figs. 17-21, respectively.

There are several points to make with respect to these figures. The first point is that the elastic scattering is larger for the excited-state case than it is for the ground-state case. This is a reasonable result because the target nucleus, in the collective-model picture, is larger in the excited state than it is in the ground state. Second, cross sections which depend strongly upon the absorptive potential differ for the two potentials considered because the absorptive potentials are, in certain energy ranges, somewhat different. Thus, cross-section differences between excited-state and ground-state cases are somewhat different, for the two potentials considered, in the cases of the total, reaction, and compound nucleus cross sections, shown in Figs. 17, 19, and 21, respectively, whereas these differences are quite similar in the cases of the elastic and direct-inelastic cross sections shown in Figs. 18 and 20. Note, however, that the trends predicted by the two potentials are very similar for every cross section calculated except for that of the total cross section. The third point is that our results for the compound nucleus formation cross

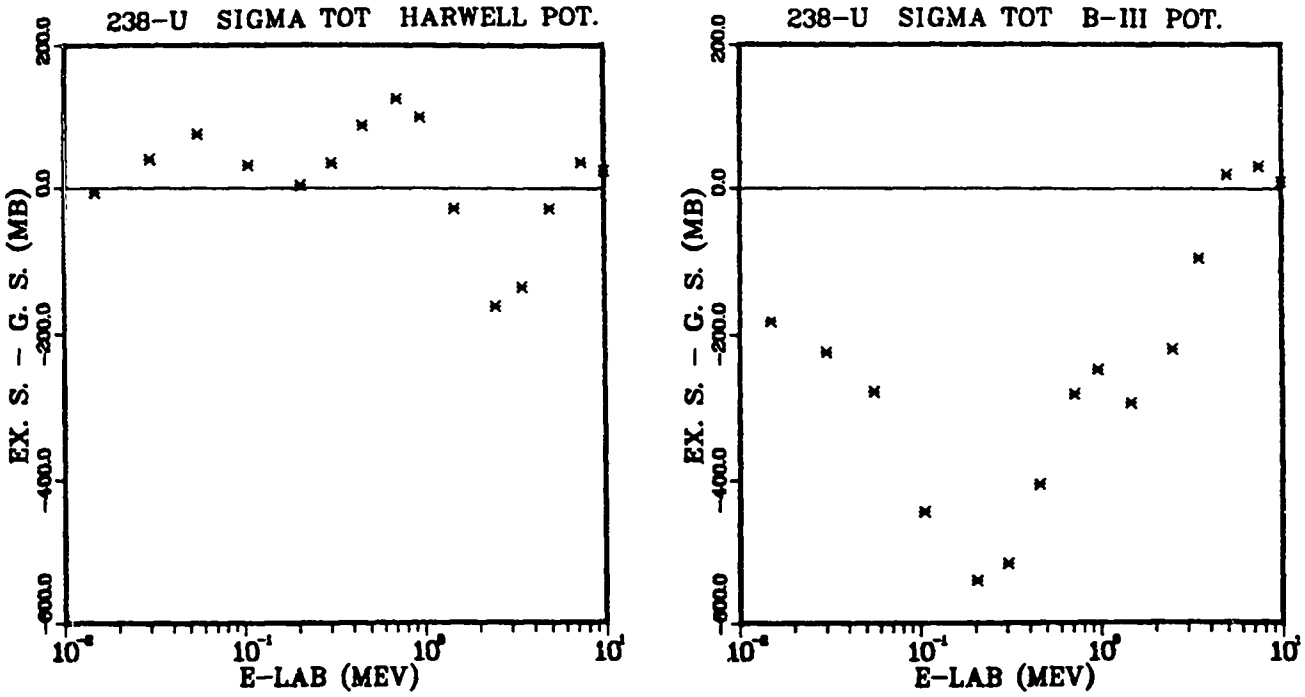

Fig. 17.
Differences between first excited-state and ground-state total cross sections for ^{238}U calculated with the Harwell potential (Ref. 28) and the B-III potential (Ref. 29).

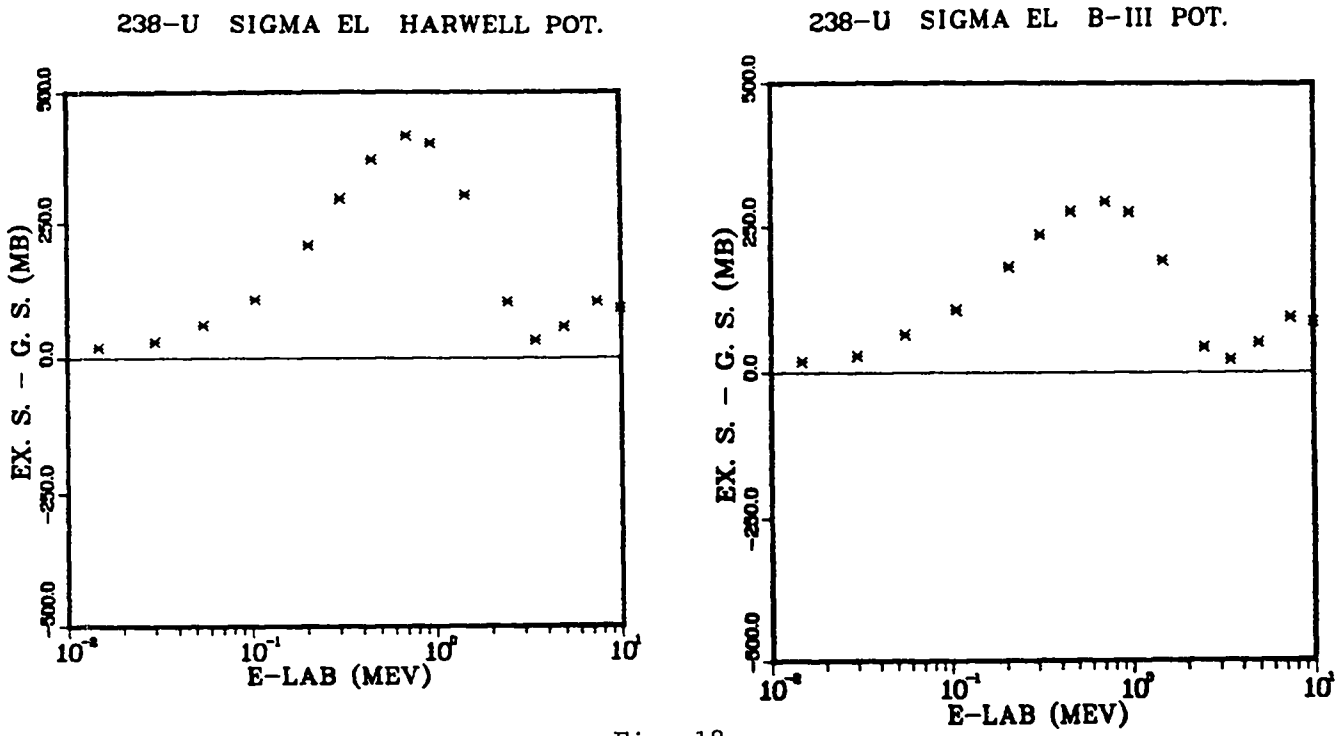

Fig. 18.
Differences between first excited-state and ground-state elastic cross sections for ^{238}U calculated with the Harwell potential (Ref. 28) and the B-III potential (Ref. 29).

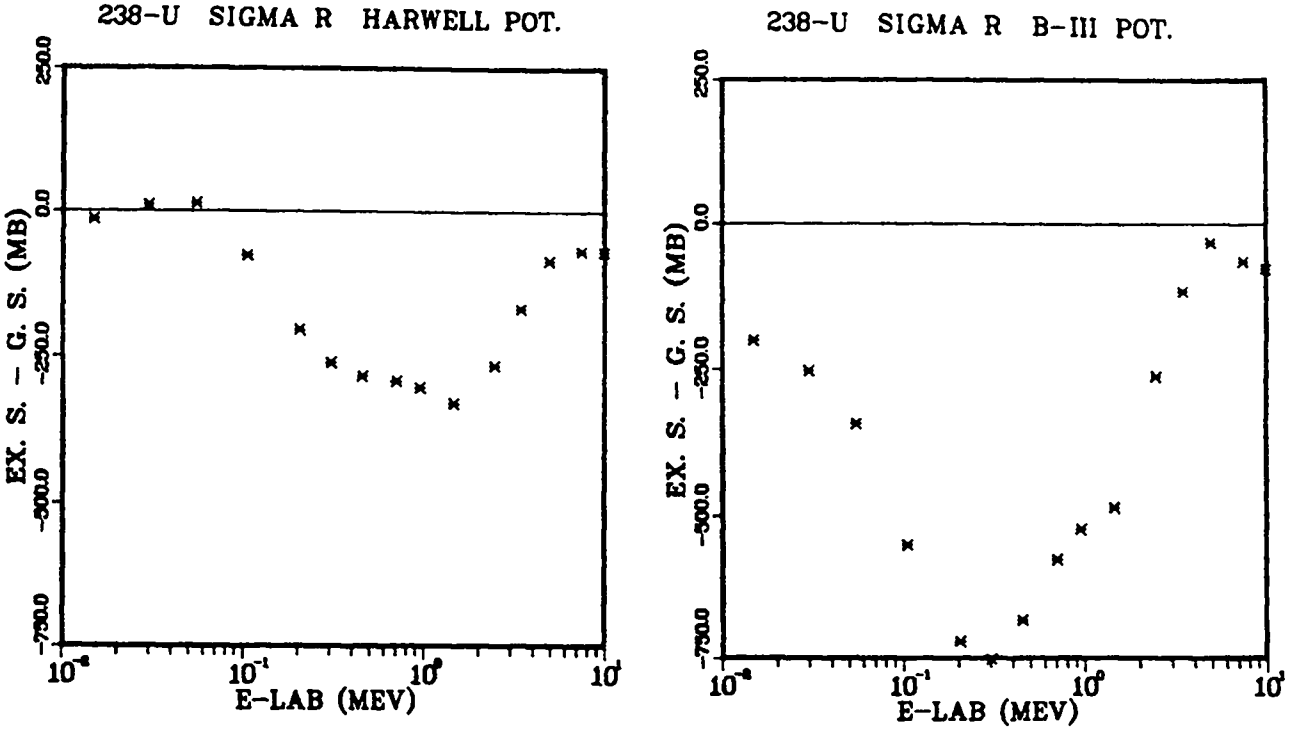

Fig. 19.
Differences between first excited-state and ground-state reaction cross sections for ^{238}U calculated with the Harwell potential (Ref. 28) and the B-III potential (Ref. 29).

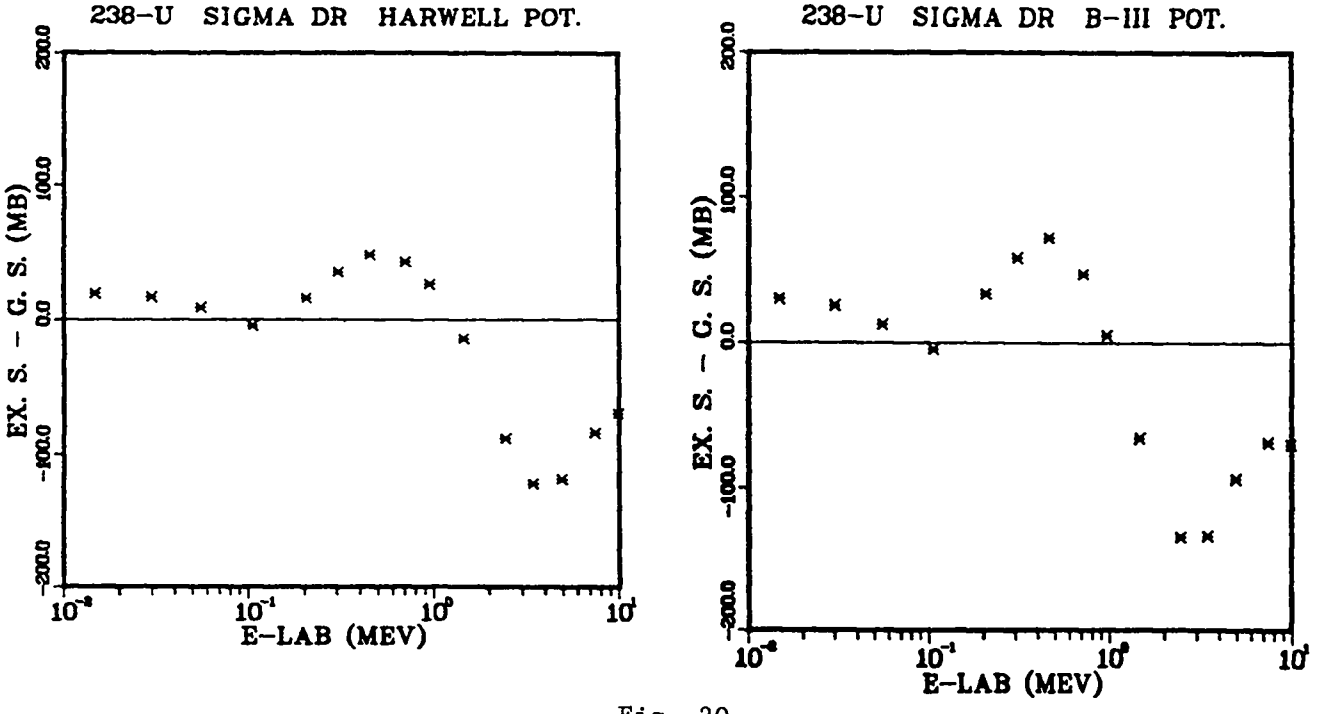

Fig. 20.
Differences between first-excited state and ground-state direct-inelastic cross sections for ^{238}U calculated with the Harwell potential (Ref. 28) and the B-III potential (Ref. 29).

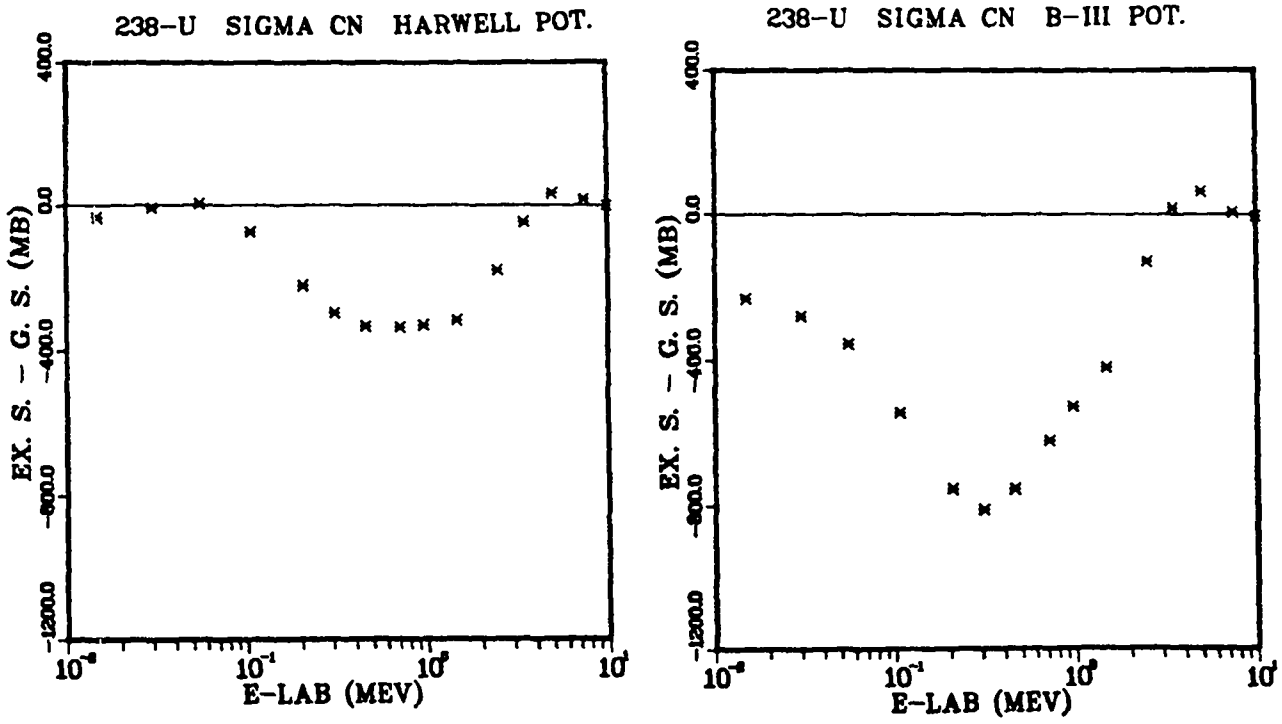

Fig. 21.
Differences between first excited-state and ground-state compound-nucleus cross sections for ^{238}U calculated with the Harwell potential (Ref. 28) and the B-III potential (Ref. 29).

section differences shown in Fig. 21 imply that possibly the fission cross section near threshold for the excited-state target is, in this particular case, less than the fission cross section near threshold for the target in its ground state.

Our next step is to repeat these same calculations using four coupled states to test the convergence of the present calculations.

H. Support Calculation for Possible NTS Antineutrino Experiments (P. G. Young)

In support of possible experiments at the Nevada Test Site (NTS) to search for antineutrino oscillations, we have developed a computer code to calculate relative antineutrino counting rates and spectra in 2-detector experiments given an antineutrino spectrum from a fission pulse source. The code has been used to investigate the sensitivity of experiments to source antineutrino spectra, to calculate energy spectra of antineutrinos in detectors for various distances and oscillation lengths, and to map out the regions of sensitivity of different experimental configurations and detector strengths.

1. NUSENS Code .

A desirable goal for oscillation experiments is to directly measure the antineutrino spectrum in a detector. Because of counting rate limitations, however, it is also necessary to consider possible experiments in which the ratio of total counts measured in two detectors located at different distances from a fission pulse is used to infer the presence of oscillations. Accordingly, a computer code called NUSENS was written to calculate relative counting rates and spectra in two antineutrino detectors located at different distances from a source.

The counting rate in detector i is given by

$$C_i \propto \bar{\sigma}_i \, N_i / r_i^2 \quad , \tag{5}$$

where r_i is the source-detector distance, N_i is the number of antineutrinos per source fission at detector i, and $\bar{\sigma}_i$ is the average cross section for the reaction whereby the antinuetrinos are detected. If $F(E,r_i)$ represents the antineutrino spectrum at the detector in units of $\bar{\nu}$/source fission/unit energy for anitneutrinos of energy E, then N_i is given by

$$N_i = \int_0^{E_m} F(E,r_i)dE \quad , \tag{6}$$

where E_m is the maximum antineutrino energy in the spectrum. For our calculations, we assumed that the $\bar{\nu}_e + p \rightarrow n + e^+$ reaction is used to detect the antineutrinos, so that the average cross section is obtained from

$$\bar{\sigma}_i = \int_0^{E_m} F(E,r_i)\sigma(E)dE \Big/ \int_0^{E_m} F(E,r_i)dE \quad , \tag{7}$$

with $\sigma(E)$ given in units of 10^{-44} cm^2 by[30]

$$\sigma(E) = 8.85 \, (E - E_{np}) \sqrt{(E - E_{np})^2 - E_e^2} \tag{8}$$

The quantity E_{np} is the neutron-proton mass difference, E_e is the electron mass, and all masses are in MeV.

The normalization for Eq. 1 was chosen such that detector 1 records a total of 10 counts at 500 m per NTS event. For our calculations we define this detector to be a "standard detector," abbreviated D_1. In the results described here, detector 2 is also taken as a standard detector, although the code has the option of varying the relative and absolute strengths of the two detectors.

For our calculations we postulate that oscillations occur between electron- and muon-type neutrinos. In this case, the probability that an electron antineutrino has not oscillated into a muon antineutrino at a distance r from its source is[31]

$$P(r) = 1 - \tfrac{1}{2} \sin^2 2\theta \, [1 - \cos (2\pi r/L)] \quad , \tag{9}$$

where θ is a mixing angle that determines the amplitude of the oscillation. The oscillation length L is given in meters by

$$L = 2.5E/\Delta m^2 \quad , \tag{10}$$

where the antineutrino energy E is in MeV and $\Delta m^2 = m_1^2 - m_2^2$ in $(eV)^2$, with m_1 and m_2 representing the eigenmasses for the electron and muon antineutrino wave functions.[31] If the antineutrino source spectrum at time t = 0 is represented by S(E), the spectrum at a detector r meters from the source is then given by

$$F(E,r) = S(E) \left\{1 - \tfrac{1}{2} \sin^2 2\theta \left[1 - \cos\left(2\pi r \frac{\Delta m^2}{2.5E}\right)\right]\right\} \quad . \tag{11}$$

The NUSENS code was written to perform the numerical integrations required in Eqs. 6 and 7 using the detector cross section from Eq. 8 and the antineutrino spectrum from Eq. 11. The ratio of counts between detectors 1 and 2 was then calculated from

$$R = C_1/C_2 = \frac{1}{\alpha} \frac{\sigma_1 N_1 r_2^2}{\sigma_2 N_2 r_1^2} \quad , \tag{12}$$

where α is the efficiency of detector 2 relative to detector 1. As stated above, a value of $\alpha = 1.0$ was used in all the present calculations.

2. Sensitivity to Source Spectrum.

To scope out the magnitude of possible effects and to investigate the sensitivity of 2-detector experiments to source spectrum, calculations were performed over a range of Δm^2 values assuming a maximum oscillation amplitude ($\theta = 45°$) and locating detectors at $R_1 = 500$ m and $R_2 = 866$ m (the range of possible values for an NTS experiment is approximately 200-1000 m). A fission antineutrino source spectrum calculated[30] for a reactor case was assumed for the base calculations. This spectrum, indicated as S(E) in Table III, was then perturbed such that the average antineutrino energy in the perturbed spectrum, S'(E') in Table III, was reduced by about 10% from the base spectrum. The perturbed spectrum was renormalized to the same total number of antineutrinos as the base spectrum. The 10% change in the antineutrino energy corresponds roughly to the difference between measurements and summation calculations of total beta energy in the 1-3 s time range after fission. Without improvement of the decay data used in summation calculations, a calculation of the antineutrino spectrum from a fission pulse would probably be considerably more uncertain than 10%.

The calculated ratios of counts between the two detectors is shown for the two assumed source spectra in Fig. 22. A pronounced oscillation away from the geometric ratio for the detectors $\left(\frac{r_1^2}{r_2^2} = 3\right)$ is seen to occur over the range $10^{-3} < \Delta m^2 < 10^{-1}$ eV^2. Note that the effect of the softer spectrum (S') is to increase the amplitude of the oscillation and to shift the oscillation to slightly lower values of Δm^2.

A tabulation of the quantities appearing in Eqs. 1-8 is given in Table IV for the above calculation using the base source spectrum S(E). The quantity Δm^2(DM**2) is tabulated in eV^2, and the average energies (EAV) are given in MeV. For Δm^2 values below 0.001 eV^2, the calculated ratio (R) is simply the geometric value 3. Similarly, for Δm^2 greater than 0.1 eV^2, the ratio returns to 3, but note that the number of detector counts (C1) is reduced by a factor of 2 from the $\Delta m^2 < 0.001$ eV^2 values. This reduction occurs because the cosine term in Eq. 11 averages to 0 for large values of Δm^2, and the average spectrum in the detector is simply $S(E)[1 - \frac{1}{2} \sin^2 2\theta]$, where we have chosen $\theta = 45°$

TABLE III

SOURCE ANTINEUTRINO SPECTRUM (E,S) AND THE MODIFIED SPECTRUM (E',S') FOR THE SENSITIVITY CALCULATIONS

E (MeV)	S(E) ($\bar{\nu}_e$/MeV-f)	E' (MeV)	S'(E') ($\bar{\nu}_e$/MeV-f)
1.000E + 00	1.560E + 00	8.000E - 01	2.707E + 00
1.500E + 00	1.350E + 00	1.200E + 00	2.342E + 00
2.000E + 00	1.050E + 00	1.600E + 00	1.822E + 00
2.500E + 00	7.660E - 01	2.000E + 00	1.329E + 00
3.000E + 00	5.720E - 01	2.400E + 00	9.924E - 01
4.000E + 00	2.690E - 01	3.200E + 00	4.667E - 01
5.000E + 00	1.020E - 01	4.000E + 00	1.770E - 01
6.000E + 00	3.500E - 02	4.800E + 00	6.073E - 02
7.000E + 00	1.010E - 02	5.600E + 00	1.752E - 02
8.000E + 00	1.870E - 03	6.400E + 00	3.244E - 03
9.000E + 00	1.000E - 50	7.200E + 00	1.735E - 50

$\bar{E}$ = 3.0 MeV $\bar{E}'$ = 2.7 MeV

TABLE IV

RESULTS OF CALCULATIONS FOR TWO DETECTORS AT 500 AND 866 m USING θ = 45° AND THE REACTOR SOURCE SPECTRUM S(E)

DM**2	C1	DC1	C2	DC2	R	DR	SIG1	SIG2	SP1	SP2	EAV1	EAV2
1.00E-06	10.0	3.16	3.3	1.83	3.000	1.897	33.6	33.6	1.66	1.66	3.00	3.00
1.00E-04	10.0	3.16	3.3	1.82	3.002	1.899	33.6	33.6	1.66	1.66	3.00	3.00
1.00E-03	9.7	3.12	3.1	1.75	3.175	2.081	34.6	36.8	1.57	1.39	3.02	3.08
2.00E-03	8.9	2.99	2.4	1.54	3.766	2.752	37.9	49.1	1.31	.81	3.11	3.41
3.00E-03	7.7	2.78	1.6	1.25	4.977	4.372	44.5	74.6	.97	.35	3.29	4.01
4.00E-03	6.3	2.52	.9	.96	6.882	7.670	56.0	51.4	.63	.30	3.59	3.22
5.00E-03	4.9	2.22	.6	.79	7.807	10.432	71.9	18.4	.38	.57	3.96	2.43
6.00E-03	3.7	1.92	.7	.82	5.490	7.295	75.3	13.0	.27	.86	3.93	2.39
7.00E-03	2.7	1.65	.9	.95	2.978	3.609	49.2	16.1	.31	.94	3.16	2.58
8.00E-03	2.1	1.45	1.2	1.10	1.727	1.969	26.0	23.5	.45	.86	2.59	2.87
1.00E-02	1.9	1.38	1.7	1.31	1.108	1.163	13.2	34.1	.81	.85	2.37	3.11
1.20E-02	2.7	1.63	2.0	1.41	1.350	1.268	15.8	35.3	.94	.94	2.56	3.02
1.50E-02	4.2	2.06	1.9	1.38	2.222	1.941	29.1	40.5	.81	.79	3.05	3.13
2.00E-02	5.8	2.41	1.6	1.27	3.590	3.186	34.3	34.7	.95	.78	3.01	3.03
2.50E-02	5.8	2.41	1.6	1.26	3.648	3.264	41.9	33.5	.77	.80	3.19	3.03
3.00E-02	5.3	2.29	1.7	1.29	3.180	2.834	33.8	34.6	.87	.80	2.94	3.04
4.00E-02	4.8	2.18	1.7	1.30	2.835	2.545	31.5	34.7	.84	.81	2.95	3.03
5.00E-02	4.9	2.22	1.6	1.28	2.984	2.685	33.4	33.7	.82	.82	3.00	3.01
6.00E-02	5.1	2.26	1.7	1.30	3.045	2.707	35.1	33.9	.81	.83	3.04	3.00
8.00E-02	5.0	2.23	1.7	1.29	2.964	2.652	33.9	33.3	.82	.84	3.01	2.98
1.00E-01	5.0	2.24	1.7	1.29	3.026	2.705	33.5	33.3	.84	.84	2.99	2.98
2.00E-01	5.0	2.24	1.7	1.29	2.993	2.675	33.3	33.6	.84	.83	2.99	2.99
5.00E-01	5.0	2.24	1.7	1.29	2.998	2.681	33.6	33.6	.83	.83	2.99	3.00
1.00E+00	5.0	2.24	1.7	1.29	3.001	2.685	33.7	33.6	.83	.83	3.00	3.00
1.00E+01	5.0	2.24	1.7	1.29	3.000	2.683	33.6	33.5	.83	.83	3.00	2.99

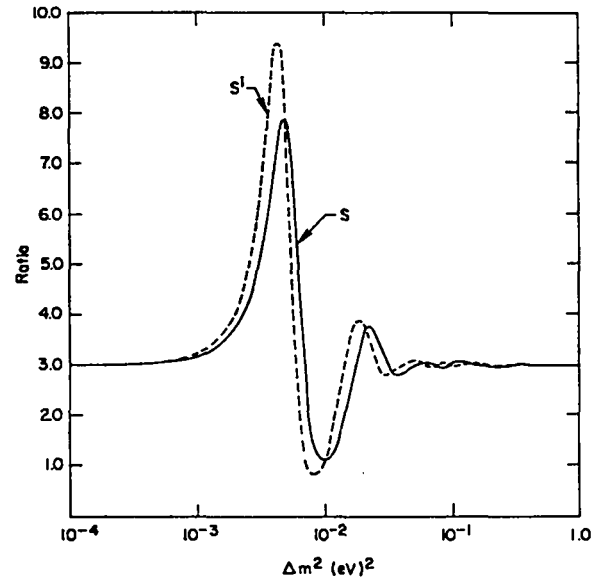

Fig. 22.
Ratio of the antineutrino counting rates in two detectors located at 500- and 866-m from a fission pulse. The mixing parameter θ is chosen to be 45°. The curves labeled S and S' correspond to different antineutrino source spectra as described in the text.

The dramatic oscillation effects near $\Delta m^2 = 0.05$ eV^2 are seen in Table IV to result from large changes in the average detection cross section at the two detectors (SIG1 and SIG2), which accompany the large variation in the average antineutrino energy in the detectors (EAV1 and EAV2). A graph of the cross-section-weighted spectrum in the 500-m detector is shown in Fig. 23 for three values of Δm^2. Clearly, a direct measurement of the antineutrino spectrum would be most useful in establishing the existence of oscillations.

3. Region of Sensitivity of an NTS Experiment.

The NUSENS code was also used to investigate the range of Δm^2 and $\sin^2 2\theta$ values over which an NTS experiment might be able to detect the presence of oscillations. For these calculations it was assumed that the only errors present are statistical in nature.

The results are given in Fig. 24, where the curves define the regions in which the ratio of counts in the detectors D_i, located at the indicated distances, would differ from the geometric value by at least two standard deviations. The region above each curve then marks the region of sensitivity for that detector-distance combination within the 2σ criterion. The subscript i on the D_i indicates multiples of our standard detector, as defined earlier. For example, the curves labeled D_5 correspond to detectors at r_1 and r_2, each having 5 times the efficiency (or size) of one standard detector. Another way of looking at the 2σ criterion is the following: the curves in Fig. 24 define the regions where, assuming antineutrino oscillations exist, there is at least a 95% probability that their existence would be indicated by that experiment.

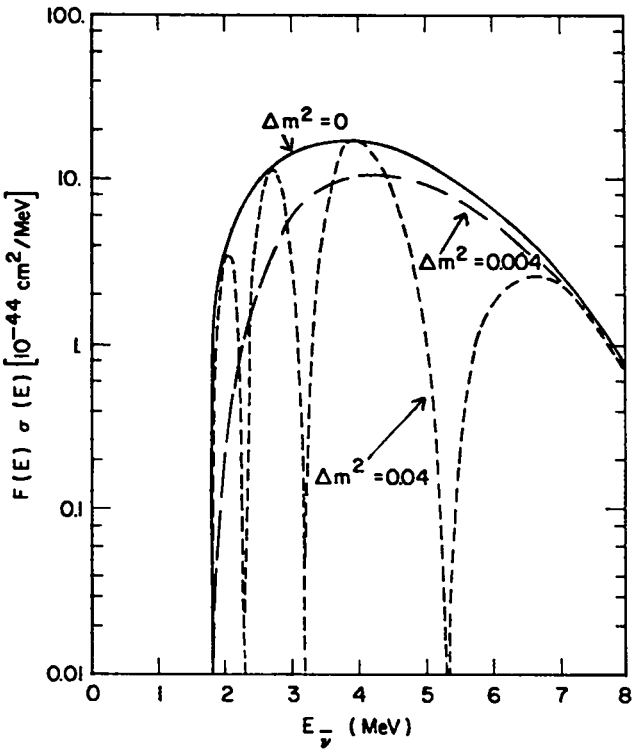

Fig. 23.
Cross-section-weighted antineutrino spectrum at a 500-m detector, assuming a mixing angle of $\theta = 45°$. The values of Δm^2 are in eV^2.

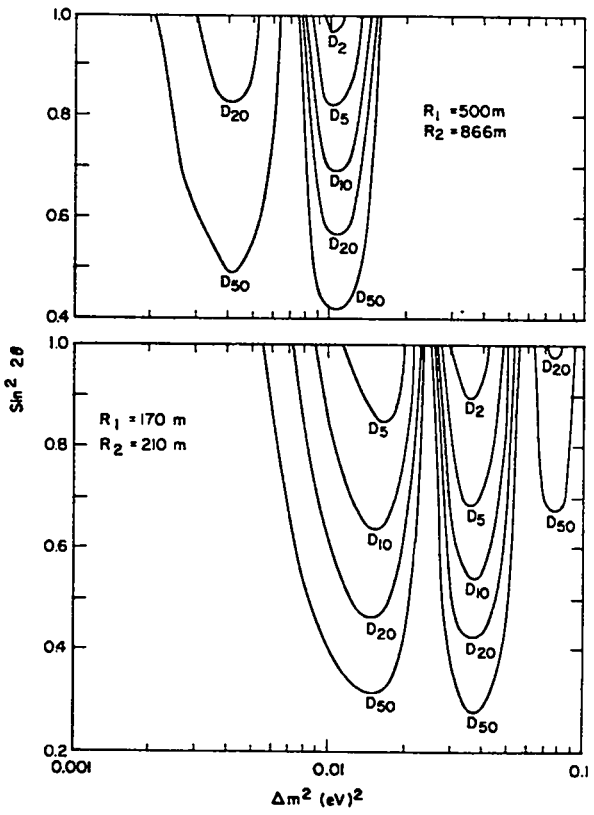

Fig. 24.
A graph of $\sin^2 2\theta$ vs Δm^2 space that various experimental arrangements would access using a 2σ criterion for significance. See the text for details.

The calculations in Fig. 24 assume equal detector efficiencies and sizes for the two detectors. Within that assumption it is clear from Fig. 24 that detectors several times the size of our standard detector (or repeated experiments) would be required to investigate any meaningful region of Δm^2 and $\sin^2 2\theta$ space. A somewhat improved situation can probably be obtained by optimizing the size of detector 2 relative to detector 1, although we have not yet made explicit calculations.

II. NUCLEAR CROSS-SECTION PROCESSING AND TESTING

A. Resonance Reconstruction in NJOY (R. E. MacFarlane, D. W. Muir, and R. M. Boicourt

The energy grid used to represent resonance cross sections in NJOY is generated in the RECONR module by successively halving the intervals between resonances, as illustrated in Fig. 25., until some kind of convergence criterion is satisfied.

We have introduced in RECONR a new user-input parameter NDIGIT, which is used to override the normal convergence criteria and terminate this subdivision process because either (1) adjacent energy values have become so closely spaced that they would round to the same number on a formatted output tape, or (2) the precision limit of the machine has been reached. Through the use of dynamic format construction, NJOY can write formatted output with up to NDIGIT = 7 digits (i.e., ± 1.234567 ± n)in an 11-column field. If binary interface files are used on a long-word machine such as CDC7600, the code can produce up to NDIGIT = 15 significant figures. Because it has been suggested[32] that as many as 9 digits may be needed for some isotopes such as ^{238}U, it is important to determine the effects of digit truncation in RECONR.

In addition to this problem, another difficulty with resonance reconstruction is that a very large number of energy grid points may arise from straightforward linear reconstruction of the resonance cross sections to some specified tolerance ERR. Many of these points come from narrow, weak, high-energy resonances which do not need to be treated accurately in many applications. Therefore, RECONR now has an option that allows such points to be treated with reduced precision if their contribution to the resonance integral is small.

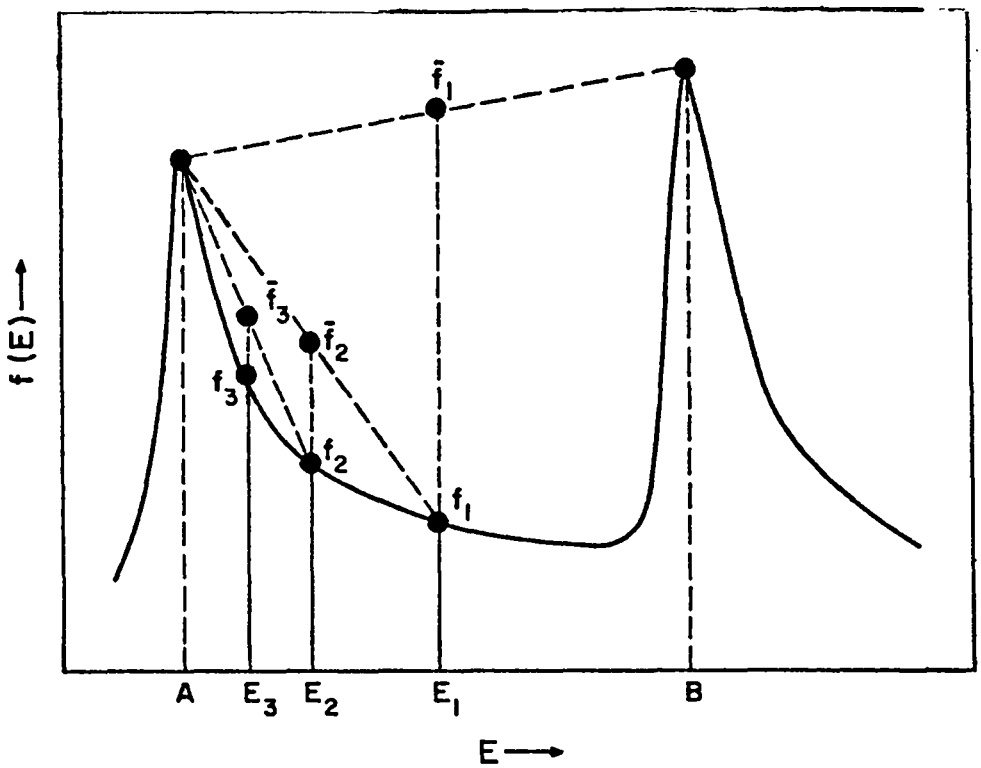

Fig. 25.
Illustration of interval-halving algorithm used in RECONR to establish energy mesh.

This integral check is carried out as follows. First, panels are subdivided until the elastic and capture cross sections are converged to within ERRMAX, where ERRMAX $\geq$ ERR. These two tolerances are usually chosen to form a reasonable band, such as 10% and 0.5% and ERRMAX ensures that every resonance is treated at least reasonably well (e.g., for plotting). If the resonance integral in a particular panel is large, the panel is further subdivided to achieve an accuracy of ERR. However, if the contribution to the resonance integral from any one interval gets small, the interval is declared converged before a local accuracy of ERR is reached.

It would be useful if the smallness of each contribution could be measured as a fraction of the full resonance integral, but, unfortunately, RECONR does not know the value of the resonance integral in advance. For this reason, an absolute error tolerance ERRINT is used. ERRINT is the maximum allowable error in the resonance integral in barns/point. Since important resonance integrals vary from a few barns to a few hundred barns and have around 10 000-50 000 energy points, a value of ERRINT = ERR/10 000 is reasonable. The integral check can be suppressed by setting ERRINT very small or by using ERRMAX = ERR.

When resonance reconstruction is complete, RECONR provides a summary of the possible average errors caused by the significant-figure limit and the resonance-integral check in several energy bands. An example is shown in Table V. The parameter NDIGIT, and the parameters ERRMAX and ERRINT taken together, should be considered a set of knobs that can be used to adjust the errors in their respective columns to get an appropriate balance of accuracy and computing cost for a particular application.

To get a more detailed picture of the impact of these parameters, 6 test cases were run for iron and ^{238}U. The input parameters for these 6 problems are summarized in Table VI, and gross results from the RECONR runs are given in Tables VII and VIII. Note that substantial savings are possible without much increase in error. The GROUPR module was then used to convert the cross sections for each case to multigroup form, using both 68 quarter-lethargy groups (GAM-I) and 620 groups (SAND-II), 1/E weighting, and background cross sections SIGZERO of infinity, 10 barns (^{238}U only), and 0.1 barns (Fe only).

The results for the 68-group structure are given in Tables IX and X. The reference value is obtained with NDIGIT = 7 and the resonance-integral check is suppressed. The per cent deviation of each numbered test case (see Table VI for definitions) from the reference value is also given. Energy groups containing no difference greater than 0.001% are omitted.

Perhaps the most noteworthy result of comparing Tables VII and VIII with Tables IX and X is that the 3% error estimated by the RECONR digit test in the ^{238}U capture resonance integral from 1.46-4.00 keV (see Table VIII) is a very large overestimate of the error in broad-group averages in that energy range. This is due in part to the fact that the digit-test error estimate uses only absolute values, therefore taking no credit for error cancellation between different energies (for example, peaks vs valleys). On the other hand, there is rather good correlation between the errors estimated by the resonance-integral test and the actual observed deviations from the reference case.

The results for the 620-group structure are similar with occasional larger per cent differences seen. For example, the largest difference for Case 5 in iron is 0.064%, and the largest difference for Case 5 in ^{238}U is 0.41%. Most differences are much smaller than this for both materials.

Because these two materials are among the most demanding materials to process in ENDF/B, it can be concluded that 6 (occasionally 7) digits and the default resonance-integral error criteria (ERRMAX = 20 x ERR, ERRINT = ERR/10 000) should be adequate for generating cross-section libraries.

TABLE V

EXAMPLE OF RECONR RESONANCE-RECONSTRUCTION ERROR SUMMARY (ENDF/B-V Fe)

ESTIMATED MAXIMUM ERROR DUE TO
RESONANCE INTEGRAL CHECK (ERRMAX,ERRINT)
AND SIGNIFICANT FIGURE TRUNCATION (NDIGIT)

UPPER ENERGY	ELASTIC INTEGRAL	PERCENT ERROR RES-INT	PERCENT ERROR SIG-FIG	CAPTURE INTEGRAL	PERCENT ERROR RES-INT	PERCENT ERROR SIG-FIG
1.55E+02						
4.96E+02	7.45E+00	.000	0.000	2.82E-02	.009	0.000
1.63E+03	5.94E+00	.000	0.000	1.71E-01	.002	0.000
5.20E+03	4.12E+00	.000	0.000	6.80E-03	.149	0.000
1.73E+04	6.49E+00	.000	.000	1.61E-02	.134	.008
5.62E+04	9.66E+00	.001	.000	1.74E-02	.200	.097
1.78E+05	4.20E+00	.004	.009	1.19E-02	.216	4.284
4.00E+05	3.50E+00	.008	.007	5.64E-03	.257	5.265

POINTS ADDED BY RESONANCE RECONSTRUCTION = 12309
POINTS AFFECTED BY RESONANCE INTEGRAL CHECK = 6969
POINTS AFFECTED BY SIGNIFICANT FIGURE REDUCTION = 1262
POINTS REMOVED BY BACKTHINNING = 201
FINAL NUMBER OF RESONANCE POINTS = 12749

162.036S
****

TABLE VI

DEFINITION OF RESONANCE-RECONSTRUCTION TEST CASES

Test Case	NDIGIT	ERRMAX	ERRINT
ref	7	ERR	Not used
1	7	5*ERR	ERR/10 000
2	7	20*ERR	ERR/10 000
3	7	20*ERR	ERR/1000
4	6	ERR	Not used
5	6	20*ERR	ERR/10 000

TABLE VII

GROSS RESULTS OF TESTS OF RESONANCE RECONSTRUCTION OPTIONS FOR IRON

Test Case	Resonance Points[a]	Processing Time[b]	Points Affected By Digit Test	Points Affected By Integral Test	Max Error From[c] Digit Test	Max Error From[c] Integral Test
ref	29 531	389.6	1343	0	0. %	.001%
1	16 394	224.2	276	10 946	0.	.007
2	13 126	190.5	9	8 089	0.	.009
3	8 846	145.7	1	7 373	0.	.049
4	25 963	320.3	5534	0	.009	0.
5	12 749	183.2	1262	6 969	.007	.008

a. With ERR = 0.5%
b. Includes reconstruction, 68-group averages, and 620-group averages.
c. For elastic cross section over highest 1/2 decade in resonance range (178-400 keV).

TABLE VIII

GROSS RESULTS OF TESTS OF RESONANCE RECONSTRUCTION OPTIONS FOR ^{238}U

Problem	Resonance Points[a]	Processing Time	Points Affected By Digit Test	Points Affected By Integral Test	Max Error From[c] Digit Test	Max Error From[c] Integral Test
ref	77 157	1147.5	3 588	0	.059%	0. %
1	51 363	759.3	598	22 051	.018	.045
2	46 826	719.2	558	17 676	.017	.058
3	31 327	524.1	15	19 910	0.	.283
4	61 987	972.5	17 814	0	3.06	0.
5	41 318	598.9	8 608	12 039	3.05	.029

a. With ERR = 0.5%
b. Includes RECONR reconstruction, UNRESR unresolved, 68-group averaging, and 620-group averaging
c. For capture cross section over highest 1/2 decade in resolved resonance range (1.46-4.00 keV).

TABLE IX

68-GROUP RESULTS FOR Fe ELASTIC

MATH 1326 MT 2

SIGZERO =1.000E+10

GRP	E-LOW	SIGREF	1	2	3	4	5
39	5.531E+03	8.806E+00	-.000	.000	-.001	.000	-.000
41	9.119E+03	5.215E+00	.001	.001	.006	-.000	.000
42	1.171E+04	3.119E+00	.000	.001	.001	-.000	.001
43	1.503E+04	2.037E+00	.001	.001	.003	.000	.001
44	1.930E+04	9.162E-01	.002	.004	.008	-.000	.003
46	3.183E+04	8.499E+00	.001	.001	.004	-.001	.000
47	4.087E+04	5.316E+00	.001	.001	.009	.000	.001
48	5.248E+04	4.189E+00	.001	.002	.019	.000	.003
49	6.738E+04	6.740E+00	.001	.001	.009	-.000	.001
50	8.652E+04	4.468E+00	.003	.005	.020	.001	.005
51	1.111E+05	3.601E+00	.004	.006	.024	.003	.008
52	1.426E+05	3.915E+00	.004	.005	.023	.001	.006
53	1.832E+05	4.860E+00	.005	.007	.029	-.001	.005
54	2.352E+05	2.832E+00	.008	.012	.050	.001	.013
55	3.020E+05	3.213E+00	.009	.011	.048	.001	.011
56	3.877E+05	4.263E+00	.001	.001	.003	-.000	.001

SIGZERO =1.000E-01

GRP	E-LOW	SIGREF	1	2	3	4	5
41	9.119E+03	4.996E+00	.001	.001	.005	-.000	.000
44	1.930E+04	7.917E-01	.001	.002	.002	.000	.002
45	2.479E+04	4.318E+00	.011	.013	.015	-.000	.013
46	3.183E+04	7.935E+00	.001	.001	.003	-.000	.001
47	4.087E+04	5.092E+00	.000	.001	.005	.000	.001
48	5.248E+04	3.868E+00	-.000	.000	.009	.000	.001
49	6.738E+04	2.753E+00	-.001	.000	.024	-.000	.000
50	8.652E+04	4.109E+00	.002	.004	.012	-.000	.004
51	1.111E+05	1.629E+00	.001	.003	.059	.000	.003
52	1.426E+05	2.372E+00	.004	.006	.028	-.001	.005
53	1.832E+05	2.905E+00	-.006	-.006	.007	-.001	-.007
54	2.352E+05	1.899E+00	.003	.006	.005	.000	.006
55	3.020E+05	1.612E+00	.008	.006	.043	.000	.006

TABLE X

68-GROUP RESULTS FOR ^{238}U CAPTURE

MATH 1398 MT 102

SIGZERO =1.000E+10

GRP	E-LOW	SIGREF	1	2	3	4	5
13	8.315E+00	8.640E-01	0.000	0.000	.007	.000	.000
14	1.068E+01	3.396E-01	0.000	0.000	.016	.000	.000
15	1.371E+01	4.521E-01	0.000	0.000	.003	-.000	-.000
16	1.760E+01	2.659E+02	.000	.000	.000	-.002	-.002
19	3.727E+01	2.303E+00	.000	.000	.004	.000	.000
20	4.785E+01	1.400E-01	.007	.007	.060	-.001	.006
22	7.889E+01	5.111E+00	.001	.001	.015	-.002	-.001
23	1.013E+02	4.326E+01	.000	.000	.001	-.010	-.010
24	1.301E+02	2.550E+00	.002	.002	.032	.023	.025
25	1.670E+02	1.530E+01	.000	.000	.004	-.008	-.008
26	2.145E+02	6.648E+00	.002	.002	.021	.009	.011
27	2.754E+02	4.552E+00	.003	.003	.024	-.010	-.007
28	3.536E+02	2.425E+00	.009	.011	.080	.002	.012
29	4.540E+02	3.418E+00	.007	.009	.059	-.012	-.003
30	5.829E+02	3.627E+00	.010	.012	.074	-.011	.000
31	7.485E+02	3.076E+00	.010	.012	.089	.001	.013
32	9.611E+02	2.481E+00	.020	.026	.147	-.010	.006
33	1.234E+03	1.689E+00	.029	.043	.188	-.007	.016
34	1.585E+03	1.860E+00	.021	.031	.144	-.008	.009
35	2.035E+03	1.555E+00	.034	.048	.216	-.005	.023
36	2.613E+03	1.243E+00	.057	.082	.343	-.006	.039
37	3.355E+03	1.090E+00	.038	.057	.203	.018	.050

SIGZERO =1.000E+01

GRP	E-LOW	SIGREF	1	2	3	4	5
13	8.315E+00	7.921E-01	0.000	0.000	.007	.000	.000
14	1.068E+01	3.343E-01	0.000	0.000	.016	.000	.000
15	1.371E+01	4.550E-01	0.000	0.000	.003	-.000	-.000
19	3.727E+01	1.146E+00	.000	.000	.008	.000	.000
20	4.785E+01	1.413E-01	.006	.006	.050	-.001	.005
21	6.144E+01	1.854E+00	.001	.001	.016	.000	.001
22	7.889E+01	9.377E-01	.004	.004	.061	.000	.004
23	1.013E+02	1.845E+00	.001	.001	.015	.001	.002
24	1.301E+02	3.698E-01	.015	.015	.164	-.003	.011
25	1.670E+02	9.186E-01	.005	.005	.054	.000	.005
26	2.145E+02	6.143E-01	.018	.019	.143	-.002	.016
27	2.754E+02	4.489E-01	.023	.025	.164	-.044	-.019
28	3.536E+02	3.531E-01	.049	.062	.332	.010	.070
29	4.540E+02	4.361E-01	.043	.057	.271	.012	.070
30	5.829E+02	5.045E-01	.052	.067	.301	.000	.067
31	7.485E+02	4.381E-01	.045	.060	.324	.007	.065
32	9.611E+02	4.520E-01	.078	.107	.444	.006	.090
33	1.234E+03	3.592E-01	.086	.145	.413	-.013	.093
34	1.585E+03	4.783E-01	.053	.085	.309	-.004	.063
35	2.035E+03	4.729E-01	.066	.109	.353	-.012	.080
36	2.613E+03	4.578E-01	.088	.144	.416	-.009	.115
37	3.355E+03	4.121E-01	.057	.099	.271	-.009	.075

B. SUPERX Development (R. B. Kidman)

Neutron leakage corrections to the background cross section, σ_0, and diffusion coefficient, D, were introduced in our 1976 ANS paper.[33] At that time we were dealing with ENDF/B-IV[34] data and 50 energy groups, and the effects of the leakage corrections were studied by making successive IDX[35] runs to iterate between flux (leakage) and the σ_0's and D's.

We studied the relatively leaky system ZPR-3-54 for which IDX gave an unmodified eigenvalue of 0.9322. The leakage corrections to σ_0 and D raised the eigenvalue by 0.0146 and 0.0463, respectively. The total change of 0.0609 resulted in an eigenvalue of 0.9931. (Old calculations suggest a further net correction of 0.021 to account for heterogeneity, dimensionality, and transport effects.) We also studied the less leaky system ZPR-6-7 and found that the leakage corrections increased the unmodified IDX eigenvalue from 0.9709 to 0.9747, which is a total change of only 0.0038. We concluded that the corrections were beneficial and more or less proportional to the leakage of the system.

This quarter, SUPERX (an overhauled version of IDX) was modified to accommodate the leakage corrections in a more optional, automatic fashion than was done above. Essentially, the iteration between flux (leakage) and σ_0 and D was incorporated with the already existing iteration between flux and the elastic downscatter cross section.

Before the leakage modifications, SUPERX gave an uncorrected ZPR-3-54 eigenvalue of 0.9472. This is different than the above-mentioned unmodified IDX value because we are now using 70-group ENDF/B-V data, NJOY processing and SUPERX calculations, all of which contain many changes. The leakage modification to σ_0 produced a 0.0151 increase in the ZPR-3-54 eigenvalue and a 20% increase in SUPERX running time. The leakage modification to D further produced a 0.0507 increase in the ZPR-3-54 eigenvalues and an 11% increase in SUPERX running time. The sum of the leakage modifications, therefore, raised the ZPR-3-54 eigenvalue by 0.0658 to a final uncorrected value of 1.0130, and increased the SUPERX running time by 34%. The running time increases are not very precise because we operate in a time-sharing computer environment in which the time for a particular job is somewhat dependent on the mix of other jobs running simultaneously. However, the time increases are much larger than expected and are due mainly to the necessity of repeating the f-factor calculation every flux-leakage correction iteration, and to the increased computations and more difficult convergences associated with the new D definition.

We also tested the SUPERX leakage modifications on ZPR-6-7. The initial uncorrected eigenvalue of 0.9824 increased by 0.0047 to a final value of 0.9871 with a 39% increase in running time. The past and present testing of the leakage corrections are summarized in Table XI.

The present leakage modification effects are a little larger than the effects computed earlier. The specific reason for this is not known, but generally one could probably expect different leakage modification effects if they are based on different cross sections, group structures, and code improvements. Nevertheless, the present and past effects are similar enough to assure us that the same leakage modifications have been introduced in both cases.

If one accepts the magnitude of the heterogeneity, dimensionality, and transport corrections, then the effects of the leakage modifications, which seemed to be beneficial in the past, now push the ZPR-3-54 eigenvalue too high.

Another difficulty with the complicated definition of the leakage corrected diffusion coefficient is that one can no longer generate the macroscopic diffusion coefficient for a mixture from a simple combination of microscopic isotope "diffusion coefficients." This problem is especially true in calculating isotope reactivity worths where one requires an isotope's effect on the diffusion coefficient in order to compute the isotope's leakage reactivity contribution.

These difficulties have caused us to begin a review of possible diffusion coefficient definitions. The base case definition is $D = [3 \cdot (\Sigma_{t1} - \Sigma_{s1})]^{-1}$ where Σ_{t1} and Σ_{s1} are the macroscopic current-weighted total and scattering cross sections, respectively. The base case yields a ZPR-3-54 corrected eigenvalue of 0.9833. A leakage modified diffusion coefficient yields a ZPR-3-54 corrected eigenvalue of 1.0230. Finally, a third definition $D = [3 \cdot (\Sigma_{to} - \Sigma_{s1})]^{-1}$, where Σ_{to} is the flux weighted total cross section, yields a corrected eigenvalue of 1.0253. The third definition is suggested by the simple transport approximation from one speed theory. The base case definition corresponds to the extended transport approximation for transport theory. None of the definitions give an eigenvalue very close to 1.0. In fact, a brief search of the literature has not turned up any theoretically studied or justified diffusion coefficient definition to be used with multigroup diffusion theory.

TABLE XI

TESTING LEAKAGE MODIFICATIONS

	ZPR-3-54		ZPR-6-7	
	IDX (Past)	SUPERX (Present)	IDX (Past)	SUPERX (Present)
Unmodified, uncorrected K_{eff}	0.9322	0.9472	0.9709	0.9824
Possible correction for heterogeneity, dimensionality, and transport effects	0.0210	0.0210	0.0166	0.0166
Unmodified, corrected K_{eff}	0.9532	0.9682	0.9875	0.9990
K_{eff} increase due to σ_0-leakage modification	0.0146	0.0151		
K_{eff} increase due to D-leakage modification	0.0463	0.0507		
Total K_{eff} increase due to all leakage modification	0.0609	0.0658	0.0038	0.0047
Final modified and corrected K_{eff}	1.0141	1.0340	0.9913	1.0037
Running time increase due to σ_0-leakage modification		20%		
Running time increase due to D-leakage modification		11%		
Total running time increase due to all leakage modifications		34%		39%

C. Comparison of Integral Cross Sections Calculated in Several Representations of the ^{235}U Thermal and ^{252}Cf Spontaneous Fission Spectra with Experiment (R. J. LaBauve, D. G. Madland, L. Stewart, and R. M. Boicourt)

Fifteen well-measured and documented integral reaction cross sections in the ^{235}U thermal fission spectrum, and 13 of these measured in the ^{252}Cf spontaneous fission spectrum, were used in comparison calculations for several representations of the two fission spectra. The experimental data are summarized in Ref. 36. All cross section data used in the calculations were taken from the ENDF/B-V dosimetry file.[37]

Five representations of the ^{235}U thermal fission spectrum were used in the comparison integral calculations. Included were

a. ENDF/B-V Watt spectrum[38] with thermal Watt parameters a = .988 MeV and b = 2.249 MeV,

b. the National Bureau of Standards representation,[39]

c. a new theoretical model developed at Los Alamos by Madland and Nix,[40]

d. an approximate model derived from this "exact" Madland-Nix model that is more suitable for inclusion in an evaluated data file,[41] and

e. a Watt model with parameters derived from the Madland-Nix theory; namely, a = .853 MeV and b = 4.292/MeV. Note that in the derivation of these parameters the average energy <E> was constrained to be the same as the average energy resulting from the approximate model.

The theoretical model (c), described in Ref. 40, contains the cross section for inverse compound nucleus formation, $\sigma_c(\varepsilon)$, which is obtained from optical model calculations. In the approximate theory (d), $\sigma_c(\varepsilon)$ is held constant, and the resulting fission spectrum N(E) is given by

$$\sigma_c(\varepsilon) = \text{constant}$$

$$N(E) = \frac{1}{2}[N(E,E_f^L) + N(E,E_f^H)] \quad , \tag{13}$$

where E_f^L and E_f^H are the average fission-fragment kinetic energy per nucleon of the light and heavy average fragments, respectively, and

$$N(E,E_f) = (1/3\sqrt{E_f T_m})\ [u_2^{3/2}\ E_1(u_2) - u_1^{3/2}\ E_1(u_1) + \gamma(3/2,u_2) - \gamma(3/2,u_1)]\ , \tag{14}$$

where

$$u_1 = (\sqrt{E} - \sqrt{E_f})^2/T_m\ ,$$
$$u_2 = (\sqrt{E} + \sqrt{E_f})^2/T_m\ ,$$

E_1 is the exponential integral

$$E_1(x) = \int_x^\infty \frac{e^{-u}}{u}\, du\ ,$$

γ is the incomplete gamma function

$$\gamma(a,x) = \int_0^x u^{a-1}\ e^{-u}\, du\ ,$$

and T_m is the maximum temperature of the fission-fragment residual nuclear-temperature distribution.

The initial average fragment excitation energy $\langle E^* \rangle$ and the maximum temperature T_m are related by the Fermi-gas law

$$T_m = (\langle E^* \rangle / a)^{1/2}\ , \tag{15}$$

where a is the nuclear level-density parameter. The average excitation energy is obtained from

$$\langle E^* \rangle = \langle E_r \rangle + B_n + E_n - \langle E_f^{tot} \rangle\ , \tag{16}$$

where $\langle E_r \rangle$ is the average energy release given by the difference between the ground-state mass of the fissioning compound nucleus and the ground-state masses of two average fission fragments, B_n and E_n are the separation energy and kinetic energy of the neutron inducing fission, and $\langle E_f^{tot} \rangle$ is the total average fission-fragment kinetic energy.

In this approximation, the energy dependence of the compound-nucleus formation cross section $\sigma_c(\varepsilon)$ is simulated by adjusting the value of the level-density paramter a as is currently done by setting

$$a_{eff} = A/(10\ MeV) \tag{17}$$

In the case of ^{235}U fission, masses needed in the calculation of T_m have been measured experimentally and results evaluated and tabulated.[42] This is not the case, however, for ^{252}Cf spontaneous fission, and two different mass formulas have been used in the calculation of T_m for ^{252}Cf spontaneous fission, namely, one by Moller and Nix[43] and one by Myers.[44]

A total of five representations of the ^{252}Cf spontaneous fission spectrum were used in the comparison integral calculations. Included were

a. the National Bureau of Standards representation,[39]
b. the "exact" Los Alamos representation in which the Moller-Nix mass formula was used in the calculation of T_m,
c. the "approximate" Los Alamos representation in which the Moller-Nix mass formula was used in the calculation of T_m,
d. the "exact" Los Alamos representation in which the Myers mass formula was used in the calculation of T_m, and
e. the "approximate" Los Alamos representation in which the Myers mass formula was used in calculating T_m.

The integral reaction cross section for a particular reaction,

$$\bar{\sigma}_R = \frac{\int_{E_1}^{E_2} \sigma_R(E)N(E)dE}{\int_{E_1}^{E_2} N(E)dE} , \tag{18}$$

where $\sigma_R(E)$ is the pointwise reaction cross section taken from the ENDF/B-V dosimetry file, N(E) is the spectrum represntation used, and E_1 and E_2 are the incident neutron energy limits of the ENDF/B-V file (10^{-5} eV to 20 MeV), was calculated with the NJOY code;[45] several of the integral calculations were verified using the MARK code.[46]

Results are shown in Table XII for the ^{235}U integral calculations, and in Table XIII for the ^{252}Cf calculations. Note in Table XII that all spectra give reasonable results except for the LA-Watt for reactions with high threshold energies. Agreement with experiment is also good for the ^{252}Cf spontaneous fission representations, but the Möller-Nix mass formula gives better results in the Los Alamos spectra than does the Myers formula. Note that in the case of the Los Alamos representations, better agreement with experiment could be made by adjusting the level density parameter a.

III. FISSION PRODUCTS AND ACTINIDES: YIELDS, DECAY DATA, DEPLETION, AND BUILDUP

A. Delayed Neutron Spectra [T. R. England, W. B. Wilson; R. E. Schenter, and F. M. Mann (Hanford Engineering Development Lab.)

In recent years there has been a vast improvement and increase in our knowledge of fission-product yield, cross-section and decay data. This has permitted rather accurate calculations of aggregate quantities based on the individual fission-product parameters (evaluated for ENDF/B-IV, -V) such as absorption buildup, decay power, various spectra, and even prompt and delayed neutrons ($\bar{\nu}_d$) per fission, as reported in previous progress reports and several publications.

In 1979 we also started calculating delayed neutron spectra in the conventional 6 time groups using the ENDF/B data along with experimental normalized spectra supplied by Gösta Rudstam (Sweden). These spectra are now available only for 29 of the 105 precursors, and experimental emission probabilities (Pn's) are available for 68 of the precursors. We find, however, that the 29 precursors having detailed spectra account for 70-80% of the total number of delayed neutrons, and the 68 precursors having measured Pn values account for ∿ 93% of the total. Thus, the experimental data are reasonably complete in their aggregate contributions.

Figures 26-29 show recent calculations of total and 6-group spectra out to 1 MeV (the spectra actually extend to ∿ 3 MeV). Plotted values are fractional contributions of the 29 precursor delayed neutrons per fission per 10-keV energy bin in each group and total of that calculated from the 105 precursors. The group placement of each spectrum was determined from the precursor halflife. In particular, groups 1-6 used the following halflife ranges: > 38, 14-38, >4-14, > 1.2-4, > 0.3-1.2, > 0.3 s.

TABLE XII

INTEGRAL CROSS SECTIONS(MB) IN REPRESENTATIONS OF THE ^{235}U THERMAL SPECTRUM

REACTION	THRESHOLD E IN MEV	MEASURED VALUE (PCT ERROR)	ENDF WATT CALC	ENDF WATT C/E	NBS FIT CALC	NBS FIT C/E	LA-EXACT CALC	LA-EXACT C/E	LA-APPROX CALC	LA-APPROX C/E	LA-WATT CALC	LA-WATT C/E
27AL(N,P)	1.90	3.8600 (6.5)	4.2600	1.10	4.1300	1.07	4.1900	1.09	4.3000	1.11	4.1200	1.07
27AL(N,A)	3.25	.7050 (5.7)	.7190	1.02	.6940	.98	.7180	1.02	.7190	1.02	.6060	.86
55MN(N,2N)	10.41	.2440 (6.1)	.2020	.83	.2030	.83	.2200	.90	.2040	.84	.1260	.52
59CO(N,2N)	10.64	.2270 (4.8)	.1830	.81	.1840	.81	.2000	.88	.1850	.81	.1120	.49
59CO(N,A)	5.50	.1430 (7.0)	.1500	1.05	.1450	1.01	.1490	1.04	.1500	1.05	.1240	.87
46TI(N,P)	1.62	11.8000 (6.4)	11.1700	.95	10.8100	.92	10.9600	.93	11.2800	.96	10.8100	.92
47TI(N,P)	0.00	19.0000 (7.4)	22.5000	1.18	21.6000	1.14	22.3000	1.17	22.9000	1.21	22.9000	1.21
48TI(N,P)	3.28	.3000 (6.0)	.2810	.94	.2730	.91	.2810	.94	.2820	.94	.2410	.80
54FE(N,P)	0.00	79.7000 (6.1)	81.0000	1.02	77.8000	.98	80.1000	1.01	82.5000	1.04	82.3000	1.03
56FE(N,P)	2.97	1.0350 (7.2)	1.0360	1.00	1.0070	.97	1.0270	.99	1.0390	1.00	.9260	.89
58NI(N,2N)	12.41	.0036 (6.7)	.0028	.78	.0030	.83	.0032	.89	.0029	.81	.0015	.42
58NI(N,P)	0.00	108.5000 (5.0)	105.0000	.97	100.9000	.93	104.0000	.96	107.0000	.99	107.0000	.99
63CU(N,A)	0.00	.5340 (2.8)	.5580	1.04	.5410	1.01	.5540	1.04	.5600	1.05	.5000	.94
115IN(N,N')	.34	189.0000 (4.2)	179.0000	.95	173.0000	.92	180.0000	.95	183.0000	.97	185.0000	.98
127 I(N,2N)	9.23	1.0500 (6.2)	1.2100	1.15	1.1800	1.12	1.2700	1.21	1.2200	1.16	.8300	.79
			AVERAGE -	.99		.96		1.00		1.00		.85
			<E> - 2.03		1.97		2.03		2.06		2.06	

TABLE XIII

INTEGRAL CROSS SECTIONS(MB) IN REPRESENTATIONS OF THE ^{252}CF S.F. SPECTRUM

REACTION	THRESHOLD E IN MEV	MEASURED VALUE (PCT ERROR)	NBS FIT CALC	NBS FIT C/E	LA-M/N-EXACT CALC	LA-M/N-EXACT C/E	LA-M/N-APPRX CALC	LA-M/N-APPRX C/E	LA-MYR-EXACT CALC	LA-MYR-EXACT C/E	LA-MYR-APPRX CALC	LA-MYR-APPRX C/E
27AL(N,P)	1.90	5.1000 (9.8)	5.1400	1.01	5.6200	1.10	5.6900	1.12	6.1300	1.20	6.2100	1.22
27AL(N,A)	3.25	1.0190 (2.4)	1.0590	1.04	1.0270	1.01	1.1830	1.16	1.4070	1.38	1.3810	1.36
55MN(N,2N)	10.41	.5800 (10.0)	.4400	.76	.5300	.91	.4800	.83	.6900	1.19	.6300	1.09
59CO(N,2N)	10.64	.5700 (11.0)	.4100	.72	.4900	.86	.4400	.77	.6400	1.12	.5800	1.02
59CO(N,A)	5.50	.2000 (5.0)	.2200	1.10	.2500	1.25	.2400	1.20	.2800	1.40	.2800	1.40
46TI(N,P)	1.62	14.1200 (2.6)	13.5000	.96	14.7000	1.04	14.9000	1.06	16.1000	1.14	16.3000	1.15
47TI(N,P)	0.00	19.2700 (2.5)	24.1000	1.25	25.7000	1.33	26.2000	1.36	26.8000	1.39	27.3000	1.42
48TI(N,P)	3.28	.4244 (2.8)	.4090	.96	.4650	1.10	.4560	1.07	.5400	1.27	.5300	1.25
54FE(N,P)	0.00	86.5800 (2.5)	88.3000	1.02	94.6000	1.09	96.8000	1.12	99.4000	1.15	101.7000	1.17
56FE(N,P)	2.97	1.4680 (2.8)	1.4100	.96	1.5900	1.08	1.5800	1.08	1.8000	1.23	1.7900	1.22
58NI(N,P)	0.00	115.4000 (1.9)	114.0000	.99	122.0000	1.06	125.0000	1.08	128.0000	1.11	130.5000	1.13
63CU(N,A)	0.00	.7090 (2.4)	.7580	1.07	.8500	1.20	.8440	1.19	.9970	1.41	.9610	1.36
115IN(N,N')	.34	198.3000 (2.6)	182.0000	.92	190.0000	.96	193.0000	.97	193.0000	.97	196.0000	.99
			AVERAGE -	.98		1.08		1.08		1.23		1.21
			<E> - 2.13		2.22		2.24		2.28		2.31	

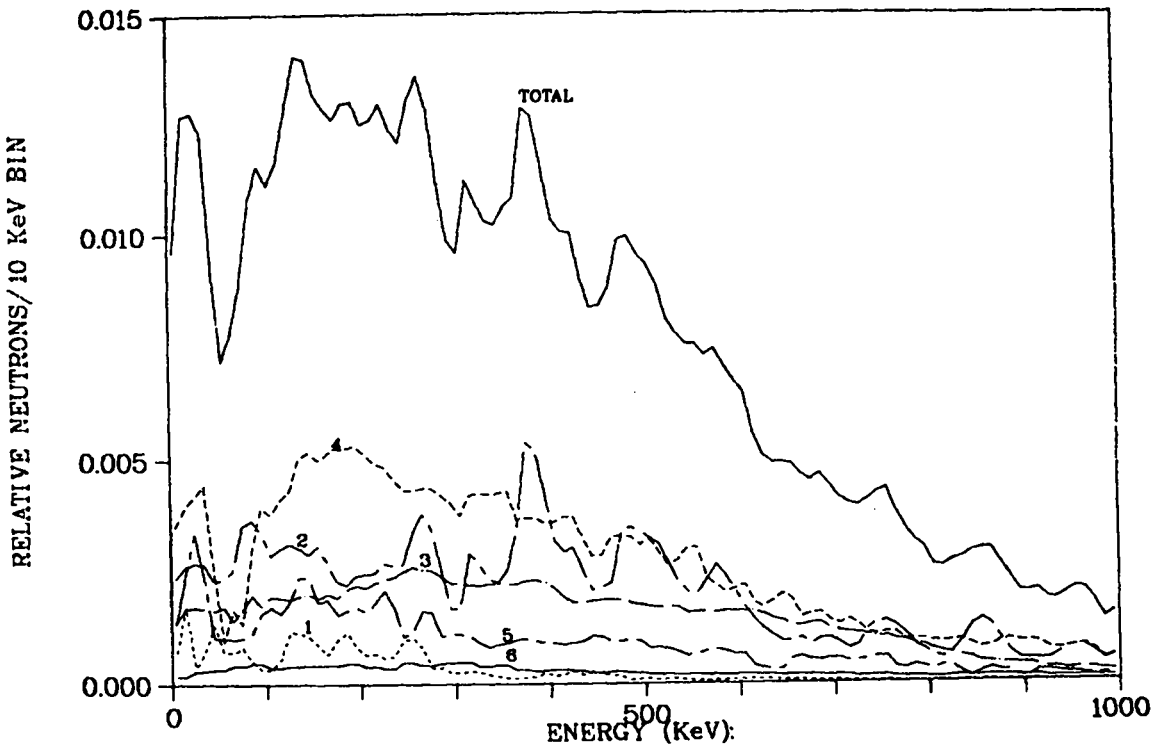

Fig. 26.

^{235}U Thermal Delayed Neutron Spectra.

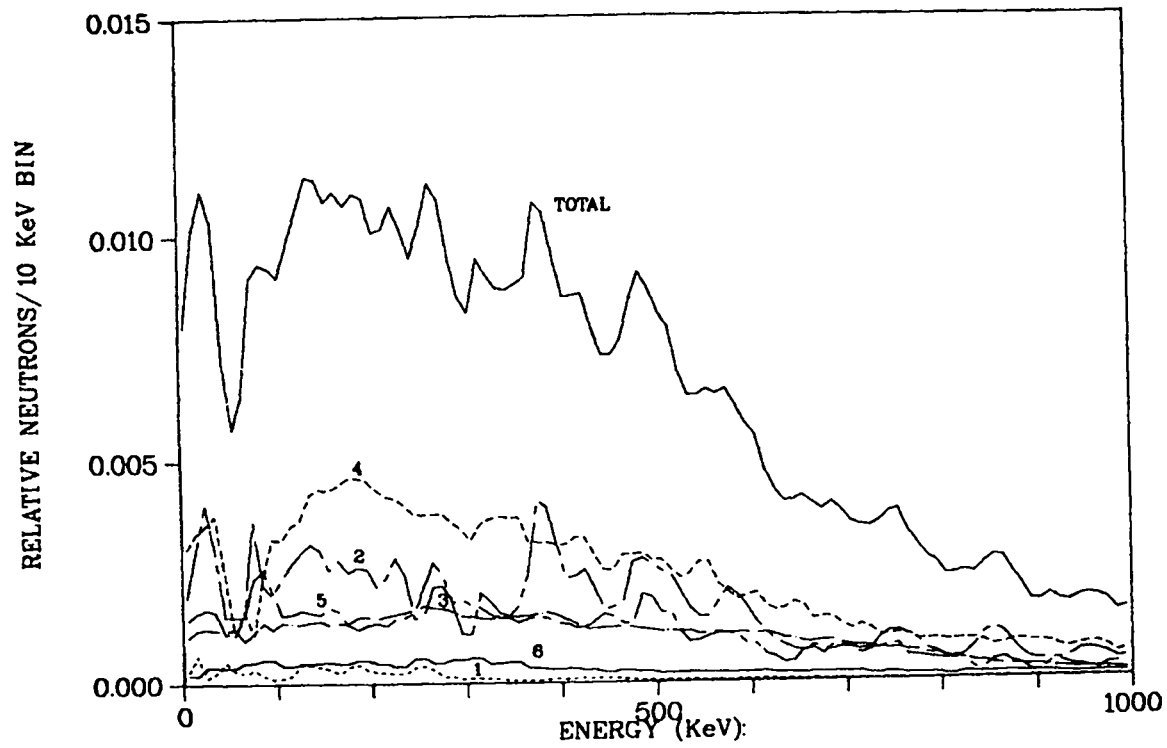

Fig. 27.

^{238}U Fast Delayed Neutron Spectra.

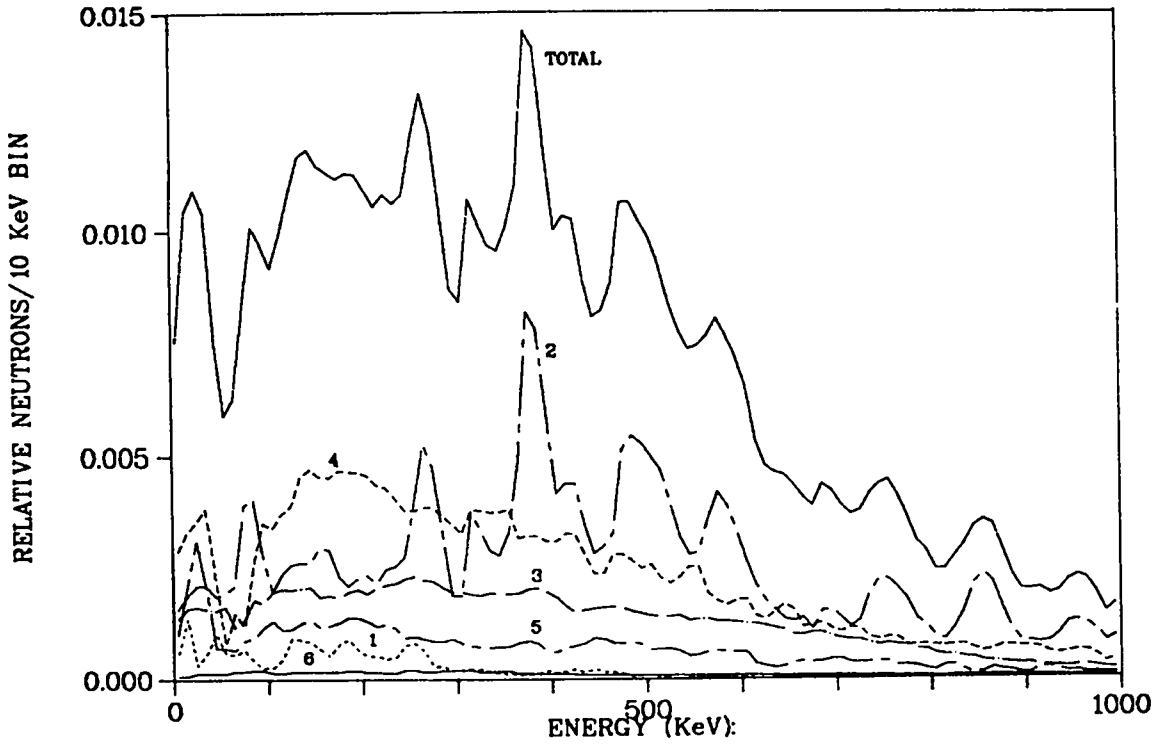

Fig. 28.

^{239}Pu Thermal Delayed Neutron Spectra.

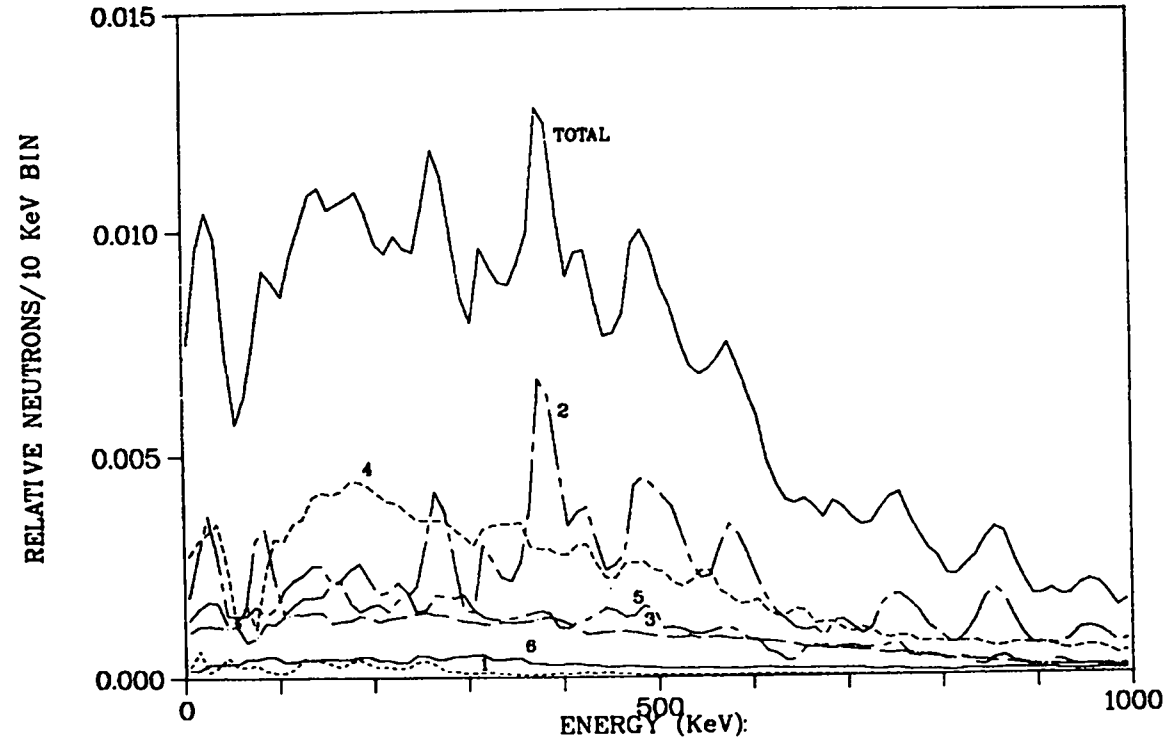

Fig. 29.

^{241}Pu Thermal Delayed Neutron Spectra.

We have made such calculations for 11 fissionable nuclides in ENDF/B-V at one or more neutron energies. Similarly, we have calculated the total $\bar{\nu}_d$ and group values from 105 precursors.[47]

We were requested to perform these calculations and to expand the data as necessary, using model calculations in a joint HEDL/Los Alamos effort by the Department of Energy. Clearly, the experimental data are nearly complete in the aggregate, but not for the individual precursors. To date, the calculations use a simple model estimate for the Pn values of 37 precursors, experimental Pn's for 68 precursors, and spectra, as noted, for 29 precursors. The ENDF/B system requires complete data if possible. To expand the spectra for the remaining 76 precursors and possibly for the 37 estimated Pn values, the BETA model code was prepared at HEDL.[48] During its preparation, it was naturally expanded to include model estimates of beta, gamma, and other spectra. In other reports (LaBauve et al.),[49,50] we show that the need for use of the BETA code for these additional spectra is probably even more important than is its use for delayed neutron precursors.

B. Preliminary Yield Data for ENDF/B-VI [T. R. England, W. B. Wilson, D. G. Madland, and B. F. Rider (General Electric Corp., Vallecitos Nuclear Ctr.)]

Preliminary evaluations of fission yields for use in ENDF/B-VI are now on a master file for 37 nuclides at one or more fission energies. There are a total of 50 sets of yields for 1176 fission products. Both independent and cumulative (by A and Z) yields plus uncertainties are in each set. The sets are listed in Table XIV and are compared with the sets available in ENDF/B-IV and -V. The evaluation for 40 sets is described in Ref. 51.

These data require expansion to cover all ENDF/B decay products in MT457, modifications to agree with the all-branching fractions and isomeric state identifications, and final conversion to the ENDF/B format. A sequence of 3 codes required for this effort are currently being updated. The preliminary evaluations also assume, as in ENDF/B-V, that the energy dependence is thermal, fast-fission (nominally 0.5 MeV), high-energy (nominally 14 MeV), or results from spontaneous fission. A few nuclides, important to analysis or irradiated fuel measurements, require additional specification of their energy dependence for the final ENDF/B-VI files.

TABLE XIV

ENDF/B FISSION-PRODUCT YIELD SETS[a]

Fissionable Nuclide	Average Energy			
	Thermal	Fast	High Energy	Spontaneous
^{227}Th	6			
^{229}Th	6			
^{232}Th		4,5,6	5,6	
^{231}Pa		6		
^{232}U		6		
^{233}U	4,5,6	5,6	5,6	
^{234}U		6	6	
^{235}U	4,5,6	4,5,6	4,5,6	
^{236}U		5,6	6	
^{237}U		6		
^{238}U		4,5,6	4,5,6	6
^{237}Np		5,6	6	
^{238}Np		6		
^{238}Pu		6		
^{239}Pu	4,5,6	4,5,6	5,6	
^{240}Pu		5,6	6	
^{241}Pu	4,5,6	5,6		
^{242}Pu		5,6		
^{241}Am	6	6	6	
^{242m}Am	6			
^{243}Am		6		
^{242}Cm		6		
^{244}Cm				6
^{245}Cm	6			
^{248}Cm				6
^{249}Cf	6			
^{250}Cf				6
^{251}Cf	6			
^{252}Cf				5,6
^{253}Es				6
^{254}Es	6			
^{254}Fm				6
^{255}Fm	6			
^{256}Fm				6

[a]The numbers 4, 5, and 6 refer to availability in ENDF/B Versions IV, V, and preliminary VI. ENDF/B-IV contains only independent yields and does not include uncertainties.

C. Formation and Testing of ENDF/B-V Based Fission-Product and Actinide Data Libraries for CINDER-2 (W. B. Wilson, T. R. England, and R. J. LaBauve)

A variety of calculations have been performed with the EPRI-CINDER[52] and CINDER-2[53] codes using ENDF/B-IV based fission-product (FP) and preliminary ENDF/B-V based actinide data libraries. The ENDF/B-IV based FP library[54] used 84 linear chains to describe 186 FP nuclides. The preliminary ENDF/B-V based actinide library[55] used 39 linear chains to describe 46 actinide nuclides. These libraries have now been modified to include ENDF/B-V data. The FP chain structure has been extended to 102 linear chains and now describes 211 FP nuclides. The combined library now includes all significant nuclide contributors to the radioactive decay power of irradiated fuel following cooling times of a few hours and all significant radionuclides considered in accessing the radiological hazards resulting from hypothetical reactor accidents.

The new combined library was formed in steps, allowing the association of changes in calculated results with the new FP chain structure and/or with the new data. Beginning with the combined library of ENDF/B-IV FP and preliminary ENDF/B-V actinide data (called here L84V4), a library L102V4 was formed from the same data base to include the new 102-chain FP chain structure. The ENDF/B-IV FP data of L102V4 were replaced with ENDF/B-V FP data to form L102V5A, and finally, the preliminary ENDF/B-V actinide data were replaced with ENDF/B-V actinide data to form L102V5B.

These four libraries were used separately in identical calculations with the CINDER-2 code to determine the nuclide inventory at the time of shutdown of 20 GWd/t PWR fuel. The input for each calculation was the 4-group history and exposure-dependent cross sections of the principal actinides (U-234-U-236, U-238, Pu-239-Pu-242), in a companion EPRI-CELL[56] calculation.

The results of the CINDER-2 calculations with the four libraries are compared in Table XV. Small variations are typically due to FP chain structure improvements and/or small cross-section, decay constant, branching-fraction or fission-yield fraction changes from ENDF/B-IV to ENDF/B-V. The nuclides added to form the new 102-chain FP structure are obvious. The principal observations made on significant variations related to data are as follows.

- The 21% decrease in Nb-95m is due to the 21% decrease in the ZR-95 decay branching fraction to Nb-95m.
- The 44% decrease in Te-125m is due to the 42% decrease in the Sb-125 decay branching fraction to Te-125m.

TABLE XV

COMPARISON OF CINDER-2 CALCULATED NUCLIDE INVENTORIES
OF 20 GWD/T PWR FUEL AT SHUTDOWN

NUCLIDE	INVENTORY (#/CC) CALCULATED WITH THE FOLLOWING LIBRARIES L84V4	L102V4	L102V5A	L102V5B
ZN 72	2.925170E-06	2.925170E-06	2.800140E-06	2.800150E-06
GA 72	8.927830E-07	8.927830E-07	8.511110E-07	8.511140E-07
GE 72	4.526360E-04	4.526360E-04	4.409890E-04	4.409900E-04
GE 73	1.472990E-03	1.472990E-03	1.577350E-03	1.577350E-03
GE 74	4.528800E-03	4.528800E-03	4.585300E-03	4.585310E-03
GE 76	4.080790E-02	4.080790E-02	4.309290E-02	4.309300E-02
GE 77	4.461330E-05	4.461330E-05	4.918380E-05	4.918390E-05
AS 75	1.348080E-02	1.348080E-02	1.371740E-02	1.371740E-02
AS 77	4.198200E-04	4.198200E-04	4.266100E-04	4.266110E-04
SE 77	9.383810E-02	9.383810E-02	9.547570E-02	9.547570E-02
SE 78	2.104700E-01	2.104700E-01	2.745910E-01	2.745910E-01
SE 79	5.931390E-01	5.931390E-01	5.516620E-01	5.516620E-01
SE 80	1.439770E+00	1.439770E+00	1.528310E+00	1.528310E+00
SE 82	3.827050E+00	3.827050E+00	3.737940E+00	3.737940E+00
BR 81	2.435610E+00	2.435610E+00	2.293970E+00	2.293970E+00
BR 82	2.745970E-04	2.745970E-04	2.511960E-04	2.511960E-04
KR 82	3.370110E-02	3.370110E-02	3.050290E-02	3.050290E-02
KR 83	5.465860E+00	5.465860E+00	5.525600E+00	5.525600E+00
KR 84	1.157260E+01	1.157260E+01	1.167410E+01	1.167420E+01
KR 85	2.931560E+00	2.931560E+00	2.933870E+00	2.933870E+00
KR85M	6.886030E-03	6.886030E-03	6.853590E-03	6.853590E-03
KR 86	2.126080E+01	2.126080E+01	2.148880E+01	2.148890E+01
KR 87		3.709220E-03	3.730120E-03	3.730120E-03
KR 88		1.163580E-02	1.162480E-02	1.162480E-02
KR 89		2.790710E-04	2.747360E-04	2.747360E-04
RB 85	1.141830E+01	1.141830E+01	1.137160E+01	1.137160E+01
RB 86		1.881940E-03	1.761350E-03	1.761350E-03
RB 87	2.761560E+01	2.761190E+01	2.784560E+01	2.784560E+01
RB 88		1.240520E-03	1.243080E-03	1.243080E-03
RB 89		1.407780E-03	1.405030E-03	1.405030E-03
SR 86		1.749590E-02	1.588070E-02	1.588070E-02
SR 88	3.947400E+01	3.945100E+01	3.934720E+01	3.934720E+01
SR 89	7.049260E+00	7.049290E+00	6.864980E+00	6.864980E+00
SR 90	6.267650E+01	6.267650E+01	6.261340E+01	6.261340E+01
SR 91	6.607810E-02	6.607810E-02	6.643770E-02	6.643770E-02
SR 92		1.954890E-02	1.954240E-02	1.954250E-02
Y 89	4.535290E+01	4.535120E+01	4.574200E+01	4.574200E+01
Y 90	1.661700E-02	1.661700E-02	1.600230E-02	1.600230E-02
Y 91	9.960550E+00	9.960550E+00	9.994680E+00	9.994680E+00
Y 92		2.553150E-02	2.573440E-02	2.573440E-02
Y 93	8.171880E-02	8.171880E-02	8.199480E-02	8.199490E-02
ZR 90	1.146540E+00	1.146540E+00	1.104310E+00	1.104310E+00
ZR 91	5.491820E+01	5.491820E+01	5.518290E+01	5.518290E+01
ZR 92	6.671200E+01	6.666690E+01	6.709250E+01	6.709260E+01
ZR 93	7.223940E+01	7.223940E+01	7.248110E+01	7.248110E+01
ZR 94	7.411080E+01	7.411080E+01	7.463910E+01	7.463920E+01
ZR 95	1.349180E+01	1.349180E+01	1.321060E+01	1.321060E+01
ZR 96	7.425480E+01	7.425480E+01	7.501020E+01	7.501020E+01
ZR 97	1.394510E-01	1.394510E-01	1.389640E-01	1.389650E-01
NB 95	7.244840E+00	7.244870E+00	7.251960E+00	7.251970E+00
NB95M		8.960210E-03	7.105310E-03	7.105320E-03
NB 97		1.024380E-02	9.928430E-03	9.928440E-03
MO 95	5.416290E+01	5.415430E+01	5.450450E+01	5.450450E+01
MO 96	1.096820E+00	1.096490E+00	1.107160E+00	1.107160E+00
MO 97	7.234180E+01	7.233170E+01	7.174770E+01	7.174780E+01
MO 98	7.164230E+01	7.164220E+01	7.172390E+01	7.172390E+01
MO 99	5.820790E-01	5.820790E-01	5.818150E-01	5.818160E-01
MO100	7.907600E+01	7.907600E+01	7.814110E+01	7.814110E+01
TC 99	7.138700E+01	7.138700E+01	7.151580E+01	7.151590E+01
TC99M	4.580430E-02	4.580430E-02	4.648800E-02	4.648810E-02

TABLE XV (Cont)

NUCLIDE	INVENTORY (#/CC) CALCULATED WITH THE FOLLOWING LIBRARIES L84V4	L102V4	L102V5A	L102V5B
RU100	4.050600E+00	4.050600E+00	3.874060E+00	3.874070E+00
RU101	6.426530E+01	6.426670E+01	6.407900E+01	6.407900E+01
RU102	5.850700E+01	5.850700E+01	5.852110E+01	5.852110E+01
RU103	5.856520E+00	5.856520E+00	5.695370E+00	5.695380E+00
RU104	3.338080E+01	3.338080E+01	3.306570E+01	3.306570E+01
RU105	1.535470E-02	1.535470E-02	1.493450E-02	1.493460E-02
RU106	9.920840E+00	9.920840E+00	9.872520E+00	9.872540E+00
RH103	3.608580E+01	3.608580E+01	3.537600E+01	3.537610E+01
RH105	1.189080E-01	1.189080E-01	1.124360E-01	1.124370E-01
PD104	6.604410E+00	6.604410E+00	6.376940E+00	6.376950E+00
PD105	2.246060E+01	2.246060E+01	2.119890E+01	2.119890E+01
PD106	5.600590E+00	5.600590E+00	6.048730E+00	6.048740E+00
PD107	8.978630E+00	8.978630E+00	8.991960E+00	8.991980E+00
PD108	5.657010E+00	5.657010E+00	5.491900E+00	5.491910E+00
PD109	9.107950E-03	9.107950E-03	1.125010E-02	1.125020E-02
PD110	1.596070E+00	1.596070E+00	1.629230E+00	1.629230E+00
PD112	1.244720E-03	1.244720E-03	1.590440E-03	1.590440E-03
AG109	2.968540E+00	2.968540E+00	3.694760E+00	3.694770E+00
AG110	3.746420E-01	3.746420E-01		
AG10M			2.464110E-02	2.464110E-02
AG111	2.543810E-02	2.543810E-02	2.711340E-02	2.711350E-02
CD110	1.799130E-01	1.799130E-01	6.492350E-01	6.492360E-01
CD111	7.884220E-01	7.884220E-01	8.415250E-01	8.415260E-01
CD112	3.942690E-01	3.942690E-01	4.838680E-01	4.838680E-01
CD113	1.380540E-02	1.380540E-02	1.337190E-02	1.337200E-02
CD114	5.367640E-01	5.367640E-01	5.990660E-01	5.990670E-01
CD115	1.319790E-03	1.319790E-03	1.320840E-03	1.320840E-03
CD15M	4.025900E-03	4.025900E-03	4.142040E-03	4.142050E-03
CD116	1.970240E-01	1.970240E-01	2.882640E-01	2.882640E-01
IN115	1.289740E-01	1.289740E-01	1.304790E-01	1.304790E-01
SN116	7.119580E-02	7.119580E-02	7.242350E-02	7.242350E-02
SN117	1.962250E-01	1.962250E-01	2.374370E-01	2.374370E-01
SN118	2.090840E-01	2.090840E-01	2.053750E-01	2.053750E-01
SN119	2.012750E-01	2.012750E-01	2.185280E-01	2.185280E-01
SN120	2.066930E-01	2.066930E-01	2.136650E-01	2.136650E-01
SN121	7.747930E-04	7.747930E-04	8.218700E-04	8.218720E-04
SN21M	1.200310E-04	1.200310E-04	2.127540E-04	2.127540E-04
SN122	2.279600E-01	2.279600E-01	2.704530E-01	2.704530E-01
SN123	5.099400E-02	5.099400E-02	1.597970E-02	1.597970E-02
SN124	3.482140E-01	3.482140E-01	4.468230E-01	4.468240E-01
SN125	1.797870E-02	1.797870E-02	6.087610E-03	6.087630E-03
SN126	9.631210E-01	9.631210E-01	1.078750E+00	1.078750E+00
SB121	2.137080E-01	2.137080E-01	2.235590E-01	2.235590E-01
SB122	1.005810E-04	1.005810E-04	1.044490E-04	1.044500E-04
SB123	2.171900E-01	2.171900E-01	2.469060E-01	2.469060E-01
SB124	9.600640E-04	9.600640E-04	1.110580E-03	1.110580E-03
SB125	4.642980E-01	4.642980E-01	4.481520E-01	4.481520E-01
SB126	5.957120E-04	5.954420E-04	2.223390E-04	2.223410E-04
SB127	2.857720E-02	2.857720E-02	2.846000E-02	2.846010E-02
SB128	3.906700E-04	3.906700E-04	3.049930E-04	3.049940E-04
SB129		5.351130E-03	5.718000E-03	5.718020E-03
TE122	5.949150E-03	5.949150E-03	6.212730E-03	6.212730E-03
TE124	2.142380E-03	2.142380E-03	2.643810E-03	2.643810E-03
TE125	7.236650E-02	7.236650E-02	7.278840E-02	7.278840E-02
TE25M	5.117560E-03	5.117560E-03	2.878680E-03	2.878680E-03
TE126	2.159600E-02	2.159620E-02	9.668590E-03	9.668610E-03
TE127	2.883510E-03	2.883510E-03	2.829440E-03	2.829450E-03
TE27M	1.178280E-01	1.178280E-01	1.203870E-01	1.203870E-01
TE128	5.362000E+00	5.362000E+00	5.142690E+00	5.142700E+00
TE129		1.353910E-03	1.461860E-03	1.461870E-03
TE29M	2.533230E-01	2.533170E-01	1.865570E-01	1.865580E-01
TE130	2.009700E+01	2.009700E+01	2.311470E+01	2.311470E+01
TE31M	1.814600E-02	1.814600E-02	2.328590E-02	2.328590E-02
TE132	5.029170E-01	5.029170E-01	5.096850E-01	5.096860E-01
TE134		6.093320E-03	6.333070E-03	6.333080E-03

TABLE XV (Cont)

NUCLIDE	INVENTORY (#/CC) CALCULATED WITH THE FOLLOWING LIBRARIES L84V4	L102V4	L102V5A	L102V5B
I127	2.081750E+00	2.081750E+00	2.029340E+00	2.029340E+00
I129	9.659130E+00	9.706910E+00	1.043510E+01	1.043510E+01
I130	4.066910E-04	4.085920E-04	1.764710E-04	1.764710E-04
I131	8.519450E-01	8.519450E-01	8.656430E-01	8.656450E-01
I132		1.488490E-02	1.517880E-02	1.517880E-02
I133	2.022270E-01	2.022270E-01	2.010040E-01	2.010040E-01
I134		9.421880E-03	9.518570E-03	9.518580E-03
I135	6.002440E-02	6.002440E-02	6.044850E-02	6.044850E-02
XE128	4.587870E-02	5.069940E-02	5.059010E-02	5.059020E-02
XE130	1.452400E-01	1.457710E-01	1.583730E-01	1.583730E-01
XE131	3.083790E+01	3.083790E+01	3.069800E+01	3.069800E+01
XE132	5.989390E+01	5.987900E+01	6.136180E+01	6.136180E+01
XE133	1.233310E+00	1.233370E+00	1.215830E+00	1.215830E+00
XE33M	7.357230E-02	7.359750E-02	1.545820E-02	1.545820E-02
XE134	9.438180E+01	9.396070E+01	9.617290E+01	9.617290E+01
XE135	2.996150E-02	2.996140E-02	2.996270E-02	2.996270E-02
XE35M		4.415000E-04	4.920810E-04	4.920820E-04
XE136	1.328770E+02	1.328770E+02	1.335370E+02	1.335370E+02
XE137		5.602700E-04	5.549780E-04	5.549780E-04
XE138		1.997080E-03	2.042880E-03	2.042880E-03
CS133	7.728950E+01	7.729120E+01	7.673430E+01	7.673430E+01
CS134	3.548530E+00	3.548530E+00	4.006810E+00	4.006810E+00
CS135	2.850950E+01	2.850930E+01	2.860950E+01	2.860950E+01
CS136	3.316890E-02	3.316880E-02	3.702630E-02	3.702640E-02
CS137	7.710040E+01	7.709990E+01	7.652860E+01	7.652870E+01
CS138		4.773450E-03	4.952240E-03	4.952250E-03
BA134	5.692940E-01	5.692940E-01	6.420170E-01	6.420170E-01
BA136	4.919420E-01	4.919390E-01	5.348920E-01	5.348920E-01
BA137	1.265290E+00	1.265200E+00	1.263180E+00	1.263180E+00
BA138	8.176360E+01	8.175610E+01	8.153380E+01	8.153390E+01
BA139		1.243630E-02	1.223230E-02	1.223230E-02
BA140	2.679710E+00	2.679710E+00	2.668540E+00	2.668540E+00
BA141		2.474250E-03	2.439730E-03	2.439740E-03
BA142		1.405880E-03	1.382790E-03	1.382790E-03
LA139	7.807750E+01	7.806510E+01	7.683610E+01	7.683620E+01
LA140	3.553260E-01	3.553260E-01	3.539200E-01	3.539200E-01
LA141		3.152140E-02	3.164610E-02	3.164610E-02
LA142		1.239050E-02	1.228800E-02	1.228800E-02
CE140	7.385680E+01	7.385660E+01	7.341710E+01	7.341710E+01
CE141	6.357150E+00	6.357200E+00	6.279000E+00	6.279010E+00
CE142	7.083330E+01	7.081950E+01	7.011330E+01	7.011330E+01
CE143	2.612980E-01	2.612980E-01	2.581180E-01	2.581180E-01
CE144	3.502630E+01	3.602630E+01	3.592490E+01	3.592490E+01
PR141	6.434310E+01	6.430950E+01	6.355660E+01	6.355660E+01
PR142	2.113780E-03	2.112680E-03	2.047850E-03	2.047850E-03
PR143	2.569130E+00	2.569130E+00	2.534470E+00	2.534470E+00
PR145	3.184840E-02	3.184840E-02	3.147330E-02	3.147340E-02
ND142	4.218530E-01	4.214160E-01	4.090890E-01	4.090890E-01
ND143	6.017960E+01	6.017960E+01	5.954970E+01	5.954980E+01
ND144	3.515610E+01	3.515610E+01	3.501040E+01	3.501040E+01
ND145	4.486570E+01	4.486570E+01	4.438590E+01	4.438590E+01
ND146	3.888490E+01	3.888490E+01	3.842810E+01	3.842810E+01
ND147	8.471450E-01	8.471450E-01	8.418020E-01	8.418030E-01
ND148	2.146450E+01	2.146450E+01	2.103350E+01	2.103360E+01
ND150	9.199810E+00	9.199810E+00	9.102660E+00	9.102660E+00
PM147	1.657040E+01	1.657040E+01	1.636200E+01	1.636200E+01
PM148	8.672810E-02	8.672810E-02	8.345470E-02	8.345480E-02
PM48M	1.869700E-01	1.869700E-01	1.847390E-01	1.847390E-01
PM149	1.219110E-01	1.219110E-01	1.199630E-01	1.199640E-01
PM151	2.234590E-02	2.234590E-02	2.212420E-02	2.212430E-02
SM147	3.229020E+00	3.229140E+00	3.181720E+00	3.181730E+00
SM148	4.303560E+00	4.303700E+00	4.191830E+00	4.191830E+00
SM149	3.592100E-01	3.592100E-01	3.437980E-01	3.437990E-01
SM150	1.596170E+01	1.596170E+01	1.565020E+01	1.565020E+01
SM151	1.297700E+00	1.297630E+00	1.282660E+00	1.282660E+00
SM152	6.573240E+00	6.573240E+00	6.474560E+00	6.474570E+00
SM153	5.319640E-02	5.319640E-02	5.255200E-02	5.255200E-02
SM154	1.435990E+00	1.435990E+00	1.403170E+00	1.403170E+00

TABLE XV (Cont)

NUCLIDE	INVENTORY (#/CC) CALCULATED WITH THE FOLLOWING LIBRARIES L84V4	L102V4	L102V5A	L102V5B
EU151	2.229080E-03	2.229080E-03	2.203430E-03	2.203430E-03
EU153	4.492680E+00	4.492680E+00	4.627450E+00	4.627460E+00
EU154	9.379080E-01	9.379080E-01	8.012810E-01	8.012820E-01
EU155	4.700170E-01	4.700170E-01	4.343150E-01	4.343160E-01
EU156	7.932460E-02	7.932460E-02	7.444370E-02	7.444380E-02
EU157	6.163910E-04	6.163910E-04	6.028530E-04	6.028560E-04
GD154	3.227660E-02	3.227660E-02	2.737900E-02	2.737900E-02
GD155	4.294630E-03	4.294630E-03	3.848460E-03	3.848470E-03
GD156	9.332430E-01	9.332430E-01	8.950770E-01	8.950780E-01
GD157	4.237210E-03	4.237210E-03	4.105950E-03	4.105970E-03
GD158	3.801370E-01	3.801370E-01	3.700790E-01	3.700800E-01
GD159	2.182080E-04	2.182080E-04	2.143460E-04	2.143470E-04
GD160	2.586900E-02	2.586900E-02	2.549860E-02	2.549860E-02
TB159	5.965060E-02	5.965060E-02	5.853280E-02	5.853290E-02
TB160	1.402630E-03	1.402630E-03	1.392070E-03	1.392070E-03
TB161	3.854930E-04	3.854930E-04	3.764910E-04	3.764920E-04
DY160	2.026650E-03	2.026650E-03	2.015140E-03	2.015150E-03
DY161	9.538570E-03	9.538570E-03	9.284230E-03	9.284250E-03
DY162	5.964680E-03	5.964680E-03	5.833250E-03	5.833270E-03
TL208	0.	0.	0.	0.
PB208	0.	0.	0.	0.
PB212	0.	0.	0.	0.
BI212	0.	0.	0.	0.
PO216	0.	0.	0.	0.
RN220	0.	0.	0.	0.
RA224	0.	0.	0.	0.
TH228	0.	0.	0.	0.
TH231	0.	0.	0.	0.
TH232	0.	0.	0.	0.
TH233	0.	0.	0.	0.
PA231	0.	0.	0.	0.
PA232	0.	0.	0.	0.
PA233	0.	0.	0.	0.
PA234	0.	0.	0.	0.
PA34M	0.	0.	0.	0.
U232	0.	0.	0.	0.
U233	0.	0.	0.	0.
U234	1.985300E+01	1.985300E+01	1.985300E+01	1.985300E+01
U235	1.892070E+03	1.892070E+03	1.892070E+03	1.892070E+03
U236	2.393840E+02	2.393840E+02	2.393840E+02	2.393840E+02
U237	4.481900E-01	4.481900E-01	4.481900E-01	4.481760E-01
U238	5.721680E+04	5.721680E+04	5.721680E+04	5.721680E+04
U239	2.806430E-02	2.806430E-02	2.806430E-02	2.806430E-02
NP237	1.326050E+01	1.326050E+01	1.326050E+01	1.325340E+01
NP238	2.483790E-02	2.483790E-02	2.483790E-02	2.493230E-02
NP239	4.045800E+00	4.045800E+00	4.045800E+00	4.045900E+00
NP240	2.034370E-05	2.034370E-05	2.034370E-05	2.034420E-05
NP40M	3.474070E-06	3.474070E-06	3.474070E-06	3.474160E-06
PU238	1.527060E+00	1.527060E+00	1.527060E+00	1.527900E+00
PU239	2.882040E+02	2.882040E+02	2.882040E+02	2.882060E+02
PU240	5.431520E+01	5.431520E+01	5.431520E+01	5.431550E+01
PU241	3.419000E+01	3.419000E+01	3.419000E+01	3.419000E+01
PU242	4.201790E+00	4.201790E+00	4.201790E+00	4.201700E+00
PU243	9.644220E-04	9.644220E-04	9.644220E-04	9.643900E-04
AM241	5.961920E-01	5.961920E-01	5.961920E-01	5.960860E-01
AM242	9.757320E-04	9.757320E-04	9.757320E-04	9.714510E-04
AM42M	6.243430E-03	6.243430E-03	6.243430E-03	6.494770E-03
AM243	3.508550E-01	3.508550E-01	3.508550E-01	3.509150E-01
AM244	1.687620E-05	1.687620E-05	1.687620E-05	1.446390E-05
AM44M	9.718760E-06	9.718760E-06	9.718760E-06	9.823870E-06
CM242	7.232210E-02	7.232210E-02	7.232210E-02	7.200290E-02
CM243	7.905400E-04	7.905400E-04	7.905400E-04	7.913460E-04
CM244	3.669470E-02	3.669470E-02	3.669470E-02	3.669860E-02
CM245	9.005480E-04	9.005480E-04	9.005480E-04	9.016190E-04
CM246	2.823700E-05	2.823700E-05	2.823700E-05	2.830530E-05

- o The 252-day and 24.6-s states of AG-110, designated respectively as Ag-110g and Ag-110m in ENDF/B-IV, are reversed in designation in ENDF/B-V; the Ag-109 neutron absorption branching fractions used in their formation remain 95% to the ground state, resulting in a change of designation and a lower inventory of the longer lived state. This change is reflected in the increase in Cd-110 also.
- o The 26% decrease in Te-129m is due to the 30% decrease in the Sb-129 decay branching fraction to Te-129m.
- o The 79% decrease in Xe-133m is due to the 79% decrease in the I-133 decay branching fraction to Xe-133m.
- o Decreases in Eu-154(15%), Gd-154(15%) and Gd-155(10%) are due largely to the changes in the Eu-153 thermal cross section (50% decrease) and resonance integral (5% increase).
- o Cumulative yield fraction changes from ENDF/B-IV to ENDF/B-V have resulted in notable inventory changes for Pd-109, Pd-112, Ag-109, Cd-110, Cd-112, Cd-114, Cd-116, Sn-117, Sn-121m, Sn-122, Sn-123, Sn-124, Sn-125, Sb-124 Sb-126, Sb-128, Te-124, Te-126, Te-131m, and I-120. The inventory changes for these 20 nuclides and their ENDF/B-IV and ENDF/B-V cumulative yield fractions are given in Table XVI.
- o Large inventory changes for some higher actinide nuclides have been observed because of order-of-magnitude decreases in some actinide cross sections.

The thorium-cycle nuclides Th-231-U-233 and U-232 decay products Tl-208-Th-228 have zero concentrations in these uranium cycle fuel calculations, although traces of these nuclides may be generated from higher actinide decay. Work is in progress on a new ENDF/B-V based actinide library describing the production and decay of 144 actinide nuclides covering the range Hg-206-Fm-258.[53]

TABLE XVI

COMPARISON OF ENDF/B-IV AND ENDF/B-V CUMULATIVE YIELD FRACTIONS

NUCLIDE	U235(THERM)		U238(FAST)		PU239(THERM)		PU241(THERM)		INVENTORY
	V4	V5	V4	V5	V4	V5	V4	V5	CHANGE, %
PD109	3.00-4	3.44-4	2.83-3	2.64-3	1.41-2	1.88-2	2.28-2	1.91-2	+ 24
PD112	1.27-4	1.60-4	5.13-4	6.50-4	1.07-3	1.33-3	2.30-3	2.31-3	+ 28
AG109	3.00-4	3.44-4	2.83-3	2.64-3	1.41-2	1.88-2	2.28-2	1.91-2	+ 24
CD110	5.4-11	2.54-9	9.8-13	8.8-11	2.41-8	3.83-7	3.61-8	2.46-8	+261
CD112	1.28-4	1.61-4	5.1-14	6.50-4	1.07-3	1.33-3	2.30-3	2.31-2	+ 23
CD114	1.13-4	1.40-4	4.11-4	3.93-4	4.68-4	6.06-4	7.55-4	7.25-4	+ 12
CD116	1.06-4	1.69-4	3.80-4	4.16-4	3.43-4	4.95-4	3.00-4	2.86-4	+ 46
SN117	1.08-2	1.09-4	3.61-4	3.67-4	3.43-4	5.63-4	2.62-4	2.54-4	+ 21
SN121M	5.95-8	2.22-8	3.03-9	1.38-9	3.45-7	3.61-7	2.88-8	1.54-8	+ 77
SN122	1.33-4	1.53-4	3.68-4	3.76-4	3.80-4	5.02-4	2.36-4	2.35-4	+ 19
SN123	8.92-5	2.88-5	1.98-4	4.88-5	4.25-4	7.02-5	1.25-4	3.14-5	- 69
SN124	2.20-4	2.59-4	4.34-4	4.43-4	5.49-4	8.77-4	2.93-4	2.92-4	+ 16
SN125	2.96-4	1.23-4	5.40-4	1.22-4	1.25-4	3.66-4	4.16-4	2.11-4	- 3
SB124	6.17-8	1.24-7	1.69-9	5.4-10	8.63-7	8.22-7	1.45-8	1.25-8	+ 16
SB126	8.82-5	7.87-5	9.79-5	6.69-5	3.05-4	3.92-4	1.09-4	1.08-4	- 63
SB128	1.10-4	1.17-4	3.94-5	1.73-5	9.43-4	6.52-4	7.26-5	6.85-4	- 22
TE124	6.17-8	1.24-7	1.50-9	5.4-10	8.64-7	8.22-7	1.45-8	1.25-8	+ 23
TE126	5.79-4	5.56-4	6.98-4	6.38-4	2.00-3	2.71-3	7.71-4	7.66-4	- 55
TE131M	3.63-3	3.86-3	1.39-4	2.59-3	6.49-3	1.08-2	2.59-3	1.08-2	+ 28
I130	2.35-6	2.07-6	4.88-9	8.43-9	5.88-5	5.40-5	5.64-7	1.68-5	- 57

REFERENCES

1. G. M. Hale, "Resonance Model for Three-Body Final States," Los Alamos Scientific Laboratory report LA-7200-PR, p. 2 (April 1978).

2. E. D. Arthur, " Deformed Optical Model Analysis of n+ ^{169}Tm Reactions," Los Alamos National Laboratory report LA-9060-PR, p. 6 (December 1981).

3. J. Raynal, "Optical Model and Coupled-Channel Calculations in Nuclear Physics," International Atomic Energy Agency Report, IAEA-SMR-9/8 (1970).

4. C. L. Dunford, "A Unified Model for Analysis of Compound Nucleus Reactions," Atomics International Report AI-AEC-12931 (1970).

5. P. G. Young and E. D. Arthur, "GNASH: A Preequilibrium Statistical Nuclear-Model Code for Calculation of Cross Sections and Emission Spectra," Los Alamos Scientific Laboratory report LA-6947 (1977).

6. C. L. Dunford, "A Unified Model for Analysis of Compound Nucleus Reactions," Atomics International Report AI-AEC-12931 (1970) and Los Alamos Scientific Laboratory memorandum from C. L. Dunford to P. G. Young, T-2-9 (June 30, 1971).

7. D. L. Hill and J. A. Wheeler, "Nuclear Constitution and the Interpretation of Fission Phenomena," Phys. Rev. 89, 1102 (1953).

8. A. Gilbert and A. G. W. Cameron, "A Composite Nuclear-Level Density Formula with Shell Corrections," Can. J. Phys. 43, 1446 (1965).

9. B. B. Back, O. Hansen, H. C. Britt, and J. D. Garrett, "Fission of Doubly Even Actinide Nuclei Induced by Direct Reactions," Phys. Rev. C 9, 1924 (1974).

10. B. B. Back, H. C. Britt, O. Hansen, B. Leroux, and J. D. Garrett, "Fission of Odd-A and Doubly Odd Actinide Nuclei Induced by Direct Reactions," Phys. Rev. C 10, 1948 (1974).

11. J. E. Lynn and B. B. Back, "Sub Barrier Fission Probability for a Double-Humped Barrier," Journal of Phys. A 7, 395 (1974).

12. A. Gavron, H. C. Britt, E. Konecny, T. Weber, and T. B. Wilhelmy, "Γ_n/Γ_f for Actinide Nuclei Using (^{3}He, df) and (^{3}He,tf) Reactions," Phys. Rev. C 13, 2374 (1976).

13. S. Bjørnholm, A. Bohr, and B. R. Mottelson, "Role of Symmetry of the Nuclear Shape in Rotational Contributions to Nuclear Level Densities," Symp. on the Physics and Chemistry of Fission, Rochester, 1973, IAEA Report SM-174/205, Vol. 1, p. 367 (1973).

14. A. S. Jessen, "Recent Developments in the Theory of the Nuclear Level Density," Proc. Int. Conf. on Neutron Physics and Nuclear Data, Harwell, 1978, p. 378 (1978).

15. E. D. Arthur and D. G. Foster, Jr., "Average Neutronic Properties of 'Prompt' Fission Products," Los Alamos Scientific Laboratory report LA-8036-PR, p. 8 (September 1979).

16. D. G. Foster, Jr. and E. D. Arthur, "Average Neutronic Properties of 'Prompt ' Fission Products," Los Alamos National Laboratory report LA-8757-PR, p. 11 (March 1981).

17. D. G. Madland and J. R. Nix, "Calculation of Prompt Fission Neutron Spectra, "Trans. Am. Nucl. Soc., 32, 726 (1979).

18. D. G. Madland and J. R. Nix, "Calculation of Prompt Fission Neutron Spectra," Bull. Am. Phys. Soc., 24, 885 (1979).

19. D. G. Madland and J. R. Nix, "Calculation of Prompt Fission Neutron Spectra," Proc. Int. Conf. on Nucl. Cross Sections for Technology, Knoxville, Tenn., October 22-26, 1979 (NBS Special Publication 594, Washington, 1980) p. 788.

20. D. G. Madland and J. R. Nix, "Calculation of Neutron Spectra and Average Neutron Multiplicities from Fission, "Proc. Int. Conf. on Nucl. Phys., Berkeley, Calif. (August 24-30, 1980, Vol. I Abstracts, p. 290, Lawrence Berkeley Laboratory, Univ. of California, Berkeley 1980).

21. D. G. Madland, "Prompt Fission Neutron Spectra and $\bar{\nu}_p$," Proc. Wkshop on Evaluation Meth. and Procedures, BNL, Upton, New York, September 22-25, 1980 Vol. II, p. 861. BNL report BNL-NCS-51363 (March 1981).

22. D. G. Madland, "Calculation of the Prompt Neutron Spectrum and $\bar{\nu}_p$ for the Spontaneous Fission of ^{252}Cf," Trans. Am. Nucl. Soc., 38, 649(1981).

23. D. G. Madland and J. R. Nix, "New Calculation of Prompt Fission Neutron Spectra and Average Prompt Neutron Multiplicities," submitted to Nucl. Sci. and Eng., Los Alamos preprint LA-UR-2968 (October 1981).

24. P. I. Johansson and B. Holmqvist, "An Experimental Study of the Prompt Fission Neutron Spectrum Induced by 0.5-MeV Neutrons Incident on Uranium-235," Nucl. Sci. Eng., 62, 695 (1977).

25. The experimental data shown in Fig. 16 are referenced by symbol order in Ref. 23.

26. F. D. Becchetti, Jr. and G. W. Greenlees, "Neutron-Nucleus Optical-Model Parameter A > 40, E < 50 MeV," Phys. Rev., 182, 1190 (1969).

27. D. G. Madland, "Calculation of Excited State Cross Sections for Actinide Nuclei," in Los Alamos National Laboratory report LA-8874-PR, p. 16 (July 1981).

28. D. G. Madland and P. G. Young, "Neutron-Nucleus Optical Potential for the Actinide Region," Proc. Int. Conf. on Neutron Phys. and Nucl. Data for Reactors and Other Applied Purposes, Harwell, UK, September 1978, p. 349, published by OECD (1978).

29. G. Haouat, J. Lachkar, Ch. Lagrange, Y. Patin, J. Sigaud, and R. E. Shamu, "Differential Cross Section Measurements for 3.4-MeV Neutron Scattering from ^{208}Pb, ^{232}Th, ^{235}U, ^{238}U, and ^{239}Pu," CEA report NEANDC(E) 196"L," INDC(FR) 29L, (February 1978).

30. B. R. Davis, P. Vogel, R. M. Mann, and R. E. Schenter, Phys. Rev. C 19, 2259 (1979).

31. T. J. Bowles and M. L. Silbar, Los Alamos Sci. 2, 92 (1981).

32. D. E. Cullen, "Program RECENT (version 79-1)," Lawrence Livermore National Laboratory report UCRL-50400, Vol. 17, Part C (1979).

33. R. B. Kidman, R. E. MacFarlane, and M. Becker, "A Consistent Treatment of Leakage Effects in Self-Shielding Factor Methods," Trans. Am. Nucl. Soc., Vol. 24, p. 469, November 1976.

34. D. Garber, Ed., "Data Formats and Procedure for the ENDF Neutron Cross Section Library," Brookhaven National Laboratory report BNL-50274 (1976).

35. R. W. Hardie and W. W. Little, Jr., "IDX, A One-Dimensional Diffusion Code for Generating Effective Nuclear Cross Sections," Battelle Northwest Laboratory report BNWL-954 (1969).

36. D. L. Smith, "Status of the Data Base and Some Integral-Differential Comparisons for Non-Fission Threshold Dosimetry Reactions from ENDF/B-V," NEANDC Topical Conference on Convergence of Integral and Microscopic Data, Aix-en Provence, France, April 1981.

37. B. A. Magurno, "Status of the Dosimetry File for ENDF/B-V," Proc. Advisory Group Meeting Nuclear Data for Reactor Dosimetry, INDC(nds)-103M, p. 1, Nuclear Data Section 1 Int. Atomic Energy Agency (1979).

38. M. R. Bhat, "Evaluating of ^{235}U Neutron Cross Section and Gamma Ray Production Data for ENDF/B-V," BNL-NCS-51184 (ENDF-248) March 1980.

39. J. Grundl and C. Eisenhauer, "Fission Rate Measurements for Materials Neutron Dosimetry in Reactor Environments," Proc. First ASTM-EURATOM Symp. on Reactor Dosimetry, Pettin (Holland), 1975.

40. D. G. Madland, "Prompt Fission Neutron Spectra on ν_p," Proc. Conf. on Nucl. Data Evaluations Methods and Procedures, BNL-NCS-51363, March 1981.

41. D. G. Madland, "New Fission Neutron Spectrum Representation for ENDF," Los Alamos National Laboratory Report in preparation.

42. A. H. Wapstra and K. Bos, "The 1977 Atomic Mass Evaluation," At. Data Nucl. Data Tables, 19, 175 (1977).

43. P. Moller and J. R. Nix, "Nuclear Mass Formula with a Yukawa-plus-Exponential Macroscopic Model and a Folded-Yukawa Single-Particle Potential," At. Data and Nucl. Data Tables, in press.

44. W. D. Myers, Droplet Model of Atomic Nuclei, IFI/Plenum Data Co., New York (1977).

45. R. E. MacFarlane, R. J. Barrett, D. W. Muir, and R. M. Boicourt, "The NJOY Nuclear Data Processing System: User's Manual," Los Alamos Scientific Laboratory report LA-7584-MS (1978).

46. R. E. Seamon, "Cross Sections for Monte Carlo Calculations-X-6 Activity Report," Los Alamos Scientific Laboratory report LA-8232-PR (February 1980).

47. T. R. England, R. E. Schenter, and F. Schmittroth, "Delayed Neutron Calculations using ENDF/B-V Data," Proc. ANS/APS Int. Conf. on Nuclear Cross Sections and Technology, Knoxville, Tenn., October 22-29, 1979, (NBS Special Publication 594, issued September 1980).

48. F. Mann, C. Dunn, and R. E. Schenter, "Beta Decay Properties from a Statistical Model," Trans. Am. Nucl. Soc., 39, 880 (1981).

49. R. J. LaBauve, T. R. England, D. C. George, and W. B. Wilson, Integral Testing of Evaluated Fission Product Data," Trans. Am. Nucl. Soc., 39 757, (1981).

50. R. J. LaBauve, T. R. England, and D. C. George, "Integral Data Testing of ENDF/B Fission Product Data and Comparisons of ENDF/B with Other Fission Product Data Files," Los Alamos National Laboratory report LA-9090-MS (ENDF-320) (November 1981).

51. B. F. Rider, T. R. England, D. G. Madland, J. R. Liaw, and R. E. Schenter, "Evaluation of Fission Product Yields for the U. S. National Nuclear Data Files," Proc. BNL Conf. on Evaluation Meth. and Procedures for Applied Nuclear Data , September 22-28, 1980.

52. T. R. England, W. B. Wilson, and M. G. Stamatelatos, "Fission-Product Data for Thermal Reactors, Part 2: Users' Manual for EPRI-CINDER Code and Data," Los Alamos Scientific report LA-6746-MS (December 1976). [Also published as EPRI NP-356, Part 2 (December 1976).]

53. W. B. Wilson, T. R. England, R. J. LaBauve, M. E. Battat, D. E. Wessol, and R. T. Perry, "Status of CINDER and ENDF/B-V Based Libraries for Transmutation Calculations," Proc. Int. Conf. Nucl. Waste Transmutation, Austin, Texas, July 22-24, 1980 (March 1 1981), p. 673.

54. T. R. England, W. B. Wilson, and M. G. Stamatelatos, "Fission-Product Data for Thermal Reactors, Part 1: A Data Set for EPRI-CINDER Using ENDF/B-IV," Los Alamos Scientific report LA-6745-MS (December 1976). [Also published as EPRI NP-356, Part 1 (December 1976).]

55. W. B. Wilson, T. R. England, O. Ozer, and D. E. Wessol, "Actinide Decay Power, "Trans. Am. Nucl. Soc. 32, 737 (1979).

56. "ARMP: Advanced Recycle Methodology Program," Electric Power Research Institute report CCM-3 (September 1977) (Proprietary): Chapter 5, Part II, "EPRI-CELL Code Description."

☆ U.S. GOVERNMENT PRINTING OFFICE: 1982-0-576-020/52

Printed in the United States of America
Available from
National Technical Information Service
US Department of Commerce
5285 Port Royal Road
Springfield, VA 22161

Microfiche $3.50 (A01)

Page Range	Domestic Price	NTIS Price Code	Page Range	Domestic Price	NTIS Price Code	Page Range	Domestic Price	NTIS Price Code	Page Range	Domestic Price	NTIS Price Code
001-025	$ 5.00	A02	151-175	$11.00	A08	301-325	$17.00	A14	451-475	$23.00	A20
026-050	6.00	A03	176-200	12.00	A09	326-350	18.00	A15	476-500	24.00	A21
051-075	7.00	A04	201-225	13.00	A10	351-375	19.00	A16	501-525	25.00	A22
076-100	8.00	A05	226-250	14.00	A11	376-400	20.00	A17	526-550	26.00	A23
101-125	9.00	A06	251-275	15.00	A12	401-425	21.00	A18	551-575	27.00	A24
126-150	10.00	A07	276-300	16.00	A13	426-450	22.00	A19	576-600	28.00	A25
									601-up	†	A99

†Add $1.00 for each additional 25-page increment or portion thereof from 601 pages up.

Los Alamos